



School of Chemistry

Growth of Diamond-Coated  
Nanostructures for Electrochemical  
and Bactericidal Applications

Michael Clegg

17/3/16

This thesis is submitted in partial fulfilment of the requirements for the Honours  
Degree of MSci at the University of Bristol

Supervisor: Professor Paul May

Second Assessor: Professor David Fermin

# Abstract

---

Hot filament chemical vapour deposition was used to successfully coat a selection of high surface area nanostructures in a range of boron-doped diamond films, varying in crystallinity and thickness. The nanostructures investigated were 'black-silicon' needles, both large and small, vertically aligned carbon nanotube teepees, and carbon nanotube webs. Prolonged growth of diamond onto the large silicon needles was found to produce a new porous nanostructure, called overgrown silicon needles. The films were analysed by scanning electron microscopy and Raman laser spectroscopy.

Each nanostructure was also investigated electrochemically using a potassium nitrate solution and a potassium ferricyanide solution, quantifying the capacitance, effective surface areas and diffusion coefficients of each nanostructure. The overgrown silicon needles nanostructure possessed a capacitance of  $638 \mu\text{F cm}^{-2}$  and an effective surface area of  $1544.34 \text{ mm}^2$ , the highest of all the nanostructures, and 220 times greater than a flat boron doped diamond electrode with the same geometric area ( $7 \text{ mm}^2$ ). As a result, overgrown diamond needles showed the greatest potential for applications in electrochemistry such as drug detection and water contaminant detection, demonstrating an enhanced sensitivity.

Dr H. Zanin of the University of Sao Paolo tested the nanostructures electroanalytically, confirming the overgrown silicon needles electrode as the most sensitive for electrochemical applications. This was demonstrated by detecting two biomolecules, dopamine and uric acid, at concentrations as low as  $0.27 \mu\text{M}$  and  $2.1 \mu\text{M}$  respectively.

Diamond coated small ( $1 \mu\text{m}$ ) silicon needles were shown by Dr G. Hazell of the School of Oral and Dental Sciences to display bactericidal properties, effectively killing *pseudomonas aeruginosa* bacteria. After 1 hour of incubation, the nanostructured surface effectively killed 10% more cells than a flat silicon surface, showing potential for applications as antibacterial surfaces to be utilized in hospitals and prosthetics.

# Acknowledgements

---

Firstly I would like to express my great appreciation to my supervisor Professor Paul May for his invaluable support and suggestions throughout the project, as well as his overall enthusiasm. I would also like to thank my second assessor, Professor David Fermin for his guidance in electrochemistry.

I would like to express my gratitude to Dr Gavin Hazell of the School of Oral and Dental Sciences for his work testing the samples for bactericidal properties, and for his time explaining an area of chemistry unfamiliar to me. My thanks are also extended to Dr Hudson Zanin of the University of Sao Paulo for his electrochemical analysis of the nanostructured electrodes.

Thanks are also due to Dr Verónica Celorrio and Dr Tom Risbridger for their advice on cyclic voltammetry and impedance; Dr James Smith, for showing me how to operate the laser cutter; and Jonathan Jones, for his help with scanning electron microscopy.

Finally I would like to thank everyone in the diamond and electrochemistry research groups for making the project such a fun and rewarding experience.

# Table of Contents

---

Abstract .....	1
Acknowledgements.....	2
Table of Contents .....	3
List of Figures .....	5
List of Tables .....	7
1. Introduction .....	8
1.1 Introduction to Diamond.....	8
1.2 Chemical Vapour Deposition of Diamond.....	10
1.2.1 Varying the Diamond Films.....	12
1.3 Diamond in Electrochemistry.....	13
1.3.1 Boron Doped Diamond Electrodes .....	15
1.3.1.1 Electroanalysis and Sensors .....	15
1.3.1.2 Water Treatment .....	15
1.3.1.3 Electro-synthesis.....	16
1.3.1.4 Optically Transparent Electrodes .....	17
1.3.1.5 Supercapacitors.....	17
1.4 Nanostructured Diamond Electrodes .....	18
1.4.1 Top – Down Approach .....	18
1.4.1.1 Nanohoneycomb .....	19
1.4.1.2 Nanowires .....	21
1.4.1.3 Nanoneedles.....	22
1.4.1.4 Nanowhiskers.....	23
1.4.2 Bottom–Up Approach.....	25
1.4.2.1 Vertically Aligned Carbon Nanotube Teepees .....	25
1.4.2.2 Nanorod Forests.....	26
1.4.2.3 Umbrella Structures .....	28
1.5 Antibacterial Nanostructured Surfaces .....	29
1.6 Project Objectives.....	30
2. Experimental.....	31
2.1 Electrode Fabrication .....	31

2.1.1 Substrate Preparation.....	31
2.1.1.1 Black Silicon Needles Substrates.....	31
2.1.1.2 CNT Substrates.....	31
2.1.2 Electrospray Seeding.....	31
2.1.3 Depositing a Diamond Film.....	34
2.2 Anti-Bacterial Surfaces Fabrication.....	36
2.3 Antibacterial Surface Testing.....	36
2.4 Electrochemical Analysis.....	36
2.5 Electrochemical Impedance Spectroscopy.....	38
3. Results and Discussion.....	39
3.1 Diamond Films.....	39
3.1.1 Scanning Electron Microscopy.....	40
3.1.1.1 Small Black Silicon Needles .....	40
3.1.1.2 Large Black Silicon Needles .....	41
3.1.1.3 CNT Webs .....	43
3.1.1.4 VACNT Teepees .....	44
3.1.2 Raman Spectroscopy.....	45
3.2 Electrochemistry.....	46
3.2.1 Cyclic Voltammetry .....	46
3.2.1.1 Potassium Nitrate .....	47
3.2.1.2 Potassium Ferricyanide.....	51
3.2.1.3 Dopamine and Uric Acid.....	57
3.2.2 Electrochemical Impedance Spectroscopy .....	60
3.3 Bactericidal Activity.....	63
4. Conclusions and Future Work.....	65
4.1 Conclusions.....	65
4.2 Future Work.....	66
5. References.....	68
6 Appendix	

# List of Figures

---

<b>Figure 1.1.</b> Diamond's tetrahedral structure .....	8
<b>Figure 1.2.</b> Simple schematic of CVD of diamond. ....	11
<b>Figure 1.3.</b> Cyclic voltammograms ( $100 \text{ mV s}^{-1}$ ) of a diamond and of a platinum electrode .....	14
<b>Figure 1.4.</b> Schematic diagram of a top-down approach to fabricating a nanostructured surface .....	19
<b>Figure 1.5.</b> Schematic diagram of the nanohoneycomb nanostructure fabrication process .....	20
<b>Figure 1.6.</b> SEM images of the diamond nanohoneycomb structure.....	20
<b>Figure 1.7.</b> Schematic diagram of the nanowire nanostructure fabrication process .....	21
<b>Figure 1.8.</b> AFM image of the fabricated nanowire nanostructure .....	22
<b>Figure 1.9.</b> SEM image of diamond nanoneedles .....	23
<b>Figure 1.10.</b> SEM images of diamond nanowhiskers .....	24
<b>Figure 1.11.</b> SEM images of VACNT teepees.....	25
<b>Figure 1.12.</b> Schematic diagram for the fabrication of diamond nanorod forest electrodes .....	26
<b>Figure 1.13.</b> SEM images recorded of a diamond nanoforest electrode.....	27
<b>Figure 1.14.</b> Schematic diagram for the growth of diamond microstructured umbrellas .....	28
<b>Figure 1.15.</b> SEM images of an individual diamond umbrella microstructure.....	29
<b>Figure 2.1.</b> Electrospray apparatus used to seed substrates with nanodiamond.....	32
<b>Figure 2.2.</b> Schematic diagram of the electrospray apparatus .....	33

<b>Figure 2.3.</b> Annotated picture of the substrate holder used in the HFCVD reactor. ....	34
<b>Figure 2.4.</b> Annotated photo of the reactor used for HFCVD. ....	35
<b>Figure 2.5.</b> Diagrams of the apparatus used for the first working electrode. ....	37
<b>Figure 2.6.</b> Diagram of the apparatus used for the second working electrode. ....	38
<b>Figure 3.1.</b> SEM images of the small silicon needles .....	41
<b>Figure 3.2.</b> SEM images for large silicon needles.....	42
<b>Figure 3.3.</b> SEM images of the large silicon needles with prolonged growth of diamond .....	42
<b>Figure 3.4.</b> SEM image of the overgrown silicon needles nanostructure.....	43
<b>Figure 3.5.</b> SEM images of CNT webs.....	43
<b>Figure 3.6.</b> SEM images of VACNT teepees. ....	44
<b>Figure 3.7.</b> Example green (514 nm) Raman spectrum recorded for nanocrystalline BDD film .....	46
<b>Figure 3.8.</b> Cyclic Voltammograms recorded for each nanostructure, at 50 mV/s using 0.1 M potassium nitrate solution. ....	47
<b>Figure 3.9.</b> Plots of capacitive current vs scan rate for each nanostructure. ....	49
<b>Figure 3.10.</b> SEM images used to estimate the dimensions of the large diamond-coated silicon needles .....	50
<b>Figure 3.11.</b> CVs recorded for each nanostructured electrode at different scan rates ...	52
<b>Figure 3.12.</b> Plot of peak current vs the square root of the scan rate for each nanostructure.....	53
<b>Figure 3.13.</b> CVs recorded at different scan rates in 0.1 M KCl solution containing 1 mM K <sub>3</sub> [Fe(CN) <sub>6</sub> ]. Courtesy of H. Zanin.....	56

<b>Figure 3.14.</b> Differential pulse voltammograms recorded for detecting dopamine and uric acid simultaneously. Courtesy of H. Zanin .....	57
<b>Figure 3.15.</b> Linear sweep voltammograms recorded in 0.2 M phosphate buffer solution (pH = 7.0) containing different DA concentration levels. Courtesy of H. Zanin.....	58
<b>Figure 3.16.</b> Linear sweep voltammograms recorded in 0.2 M phosphate buffer solution (pH = 7.0) containing different UA concentration levels. Courtesy of H. Zanin.....	59
<b>Figure 3.17.</b> Nyquist and Bode plots of the impedance measurements recorded for each nanostructured electrode.....	61
<b>Figure 3.18.</b> Schematic diagram of Randles circuit .....	62
<b>Figure 3.19.</b> Optical microscope images of bacteria on a flat silicon sample and a diamond coated small silicon needles sample. Courtesy of G. Hazell.....	63
<b>Figure 3.20.</b> SEM images of viable and dead bacteria cells, and cell length distribution. Courtesy of G. Hazell.....	64

## List of Tables

---

<b>Table 1.1.</b> Properties of Diamond.....	9
<b>Table 3.1.</b> Summary of films deposited onto the various substrates.....	39
<b>Table 3.2.</b> Assignments for peaks commonly observed in Raman spectra of CVD diamond films.....	45
<b>Table 3.3.</b> Capacitance and effective surface areas for each nanostructure.....	49
<b>Table 3.4.</b> Summary of the results obtained for the ferri/ferrocyanide redox system. ..	55
<b>Table 3.5</b> Analytical Sensitivity towards DA and UA. Courtesy of H. Zanin. ....	60

# 1. Introduction

---

## 1.1 Introduction to Diamond

Diamond is one of several known allotropes of carbon, including graphite, carbon nanotubes (CNT), and fullerenes, all of which differ in their bonding and structure. Unlike the other allotropes, diamond is comprised entirely of  $sp^3$  hybridised carbon atoms, arranged tetrahedrally in a repeating cubic-face centered lattice. This allows each carbon atom to form four strong carbon-carbon single bonds with its neighbouring atoms, resulting in a three dimensional, fully covalent, crystalline structure, shown in Fig 1.1.<sup>1,2</sup>

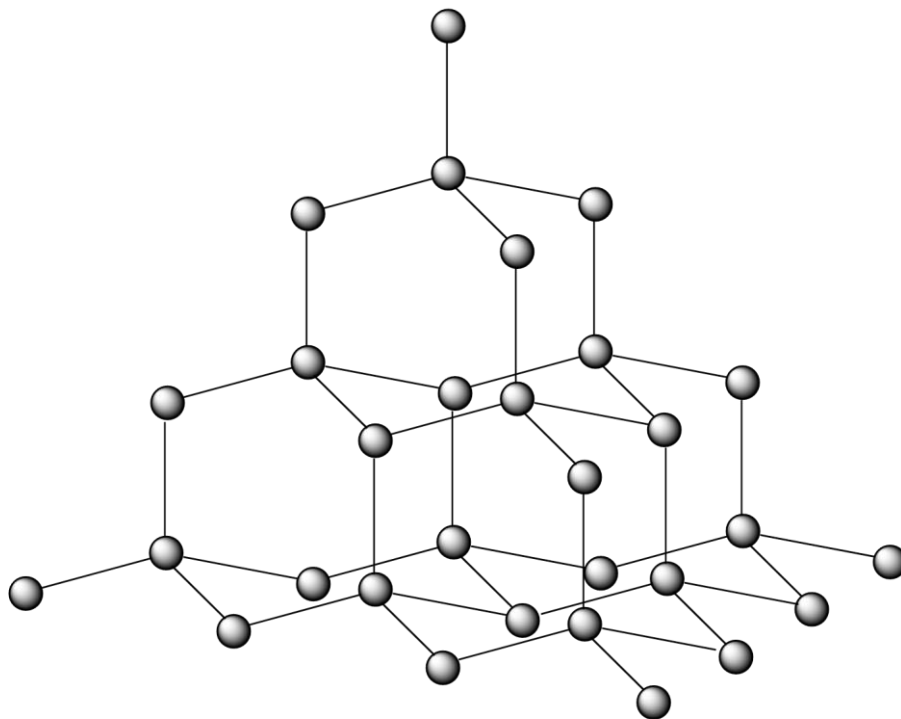


**Figure 1.1.** Diamond's tetrahedral structure, highlighting the  $sp^3$  hybridised carbon atoms and the four C-C  $\sigma$  bonds per atom.

Diamond is predominantly known for its extortionate price and its application in the gemstone industry. However, diamond actually possess several astounding, and often superlative properties, (shown in table 1.1) such as extreme mechanical hardness, the highest room temperature thermal conductivity, broad optical transparency and a negligible/negative electron affinity. These properties lend diamond to applications in cutting tools <sup>3</sup>, heat-flux sensors <sup>4</sup>, optical lenses <sup>5</sup> and field emission displays, <sup>6</sup> respectively. Unfortunately, research and applications exploiting this ‘wonder’ material were restricted due to the unavailability of natural diamond, making it economically unfeasible.

**Table 1.1.** Some of diamond’s astounding properties.

<b>Property</b>	<b>Value</b>
Extreme Hardness / (kg mm <sup>-2</sup> )	10,000
Tensile Strength / GPa	1.2
Compressive Strength / GPa	110
Young’s Modulus / GPa	1220
Thermal Conductivity / (W cm <sup>-1</sup> K <sup>-1</sup> )	20
Thermal Expansion Coefficient / K <sup>-1</sup>	1.1×10 <sup>-6</sup>
Resistivity / (Ω cm)	1×10 <sup>13</sup>
Bandgap / eV	5.45
Sound Velocity / (km s <sup>-1</sup> )	18
Biologically Compatible	-
High Resistance to Chemical Corrosion	-
Very Small/Negative Electron Affinity	-

This resulted in a flourish of interest in synthesising artificial diamond that possessed the same desired physical properties as natural diamond, but could be obtained at a much lower price.

## **1.2 Chemical Vapour Deposition of Diamond**

This was achieved using a technique known as chemical vapour deposition (CVD), which allowed for diamond to be synthesised at low pressures and temperatures, with relatively low cost. CVD of diamond involves the deposition of diamond from a hydrocarbon gas, typically methane, on to a heated substrate. Although the chemical and physical processes involved in CVD are complicated and still not completely understood, the process can be explained by the simple schematic shown in Fig. 1.2. Firstly, the gases are injected into the chamber and diffuse towards the substrate, becoming activated on the way and creating a gas-phase non-equilibrium (driving the diffusion of gas molecules towards the substrate). This gas-phase activation can be performed in several ways, however, the predominant two are thermal activation, and plasma activation, demonstrated by hot filament CVD (HFCVD) and microwave plasma-enhanced CVD (MWCVD) respectively.<sup>7</sup> Once activated the gas molecules dissociate via hydrocarbon pyrolysis and the radicals formed undergo a complex combination of heterogeneous and homogeneous gas phase reactions, resulting in nucleation of the substrate surface.<sup>8</sup> Once the nucleation density has reached a maximum, and surface nucleation has been terminated, the crystals continue to grow homogeneously outwards in all directions before adjacent crystals coalesce forming a continuous film. Once deposition has finalised, the surface atoms are hydrogen terminated, removing any reactive dangling bonds, and thus preventing the surface atoms cross-linking to form a graphite-like surface. Consequently this is a vital step in CVD and is why the hydrocarbon gas must be diluted with hydrogen.

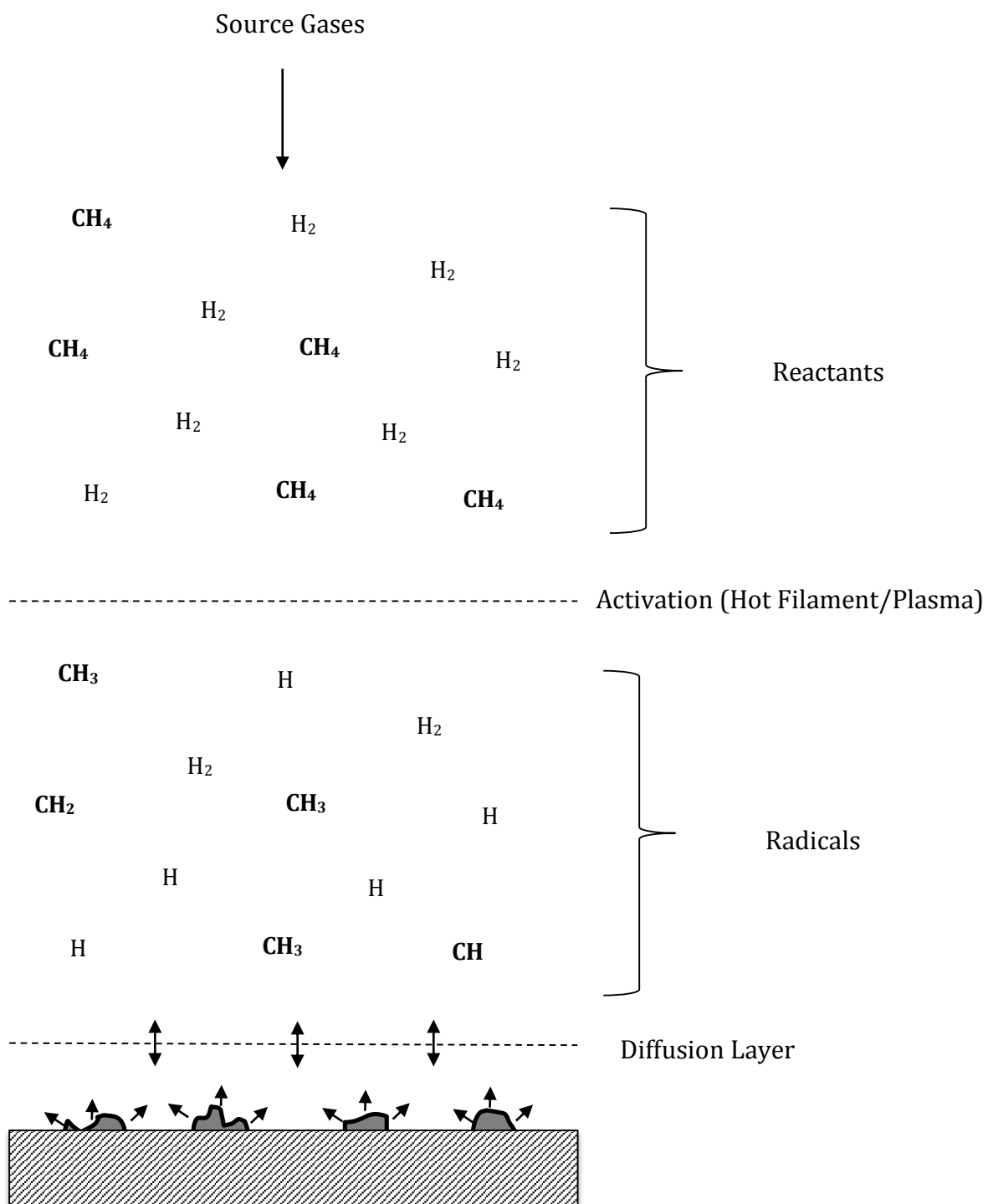


**Figure 1.2.** Simple schematic of CVD of diamond, displaying the activation of the reactant gases into radicals which then react and diffuse towards the heated substrate where diamond is deposited.

### 1.2.1 Varying the Diamond Films

The conditions used during CVD can be varied in several ways to alter the diamond films produced during the process, providing access to a range of different film properties, specialised for particular applications.<sup>9, 10, 11, 12, 13, 14, 15</sup> One parameter which is easily controlled is the grain size of the diamond film, which can be reduced from a few microns (microcrystalline diamond (MCD)) down to less than 10 nm (nanocrystalline diamond (NCD)).<sup>16</sup> There are a few ways this can be achieved, such as increasing the methane concentration from typically 1% ( $\text{CH}_4/\text{H}_2$ ) to  $\sim 5\%$ ,<sup>17</sup> reducing the pressure inside the reaction chamber to  $\sim 7$  Torr,<sup>18</sup> or by introducing a noble gas (He, Ar, Xe) to the reaction chamber typically at a noble gas/ $\text{H}_2$  ratio of  $\sim 9$ .<sup>14, 19</sup>

Another parameter easily varied is the growth rate of the diamond film. CVD of diamond is notorious for having a slow growth rate ( $\sim 1 \mu\text{m}/\text{h}$ ). This problem can be partially solved through preferential etching of graphite by using a non-diamond carbon etchant such as oxygen, fluorine, hydrogen or hydroxyl radicals.<sup>10, 20</sup> Furthermore the growth rate can be dramatically increased by using a surface pretreatment technique before deposition. Again there are a few ways in which this can be achieved including, surface abrasion using a diamond powder, or more uniformly using ultrasonic vibrations or plasmas etching;<sup>21, 22, 23, 24</sup> seeding the substrate with diamond, increasing the nucleation rate;<sup>25, 26, 27</sup> or bias enhanced nucleation, accelerating any carbon containing ions in the gas phase towards the substrate and sub-planting them beneath the surface.<sup>28</sup>

Finally a crucial parameter that can be altered is the conductivity of the diamond films. This is achieved via doping, with the most popular diamond dopant being boron. Boron doped diamond (BDD) has been shown to successfully display p-type conductivity over a wide range depending on the concentrations of boron incorporated. At low concentrations, BDD behaves as an extrinsic semiconductor, whereas at high concentrations, it behaves as a quasi-metal, displaying electrical properties comparable to that of pure metals.<sup>29</sup> This range in conductivities highlights BDD's versatility towards electrochemical applications, some of which will be discussed later. The most common way to dope diamond with boron is to introduce diborane into the gas mixture during deposition, although other methods have been reported<sup>30, 31</sup>. This method works with

HFCVD and MWCVD, and allows for the concentration of boron to be controlled by altering the flow rate of the diborane.<sup>32, 33</sup> Other successful diamond dopants include the group V elements, nitrogen<sup>34, 35</sup> and phosphorus<sup>36, 37, 38</sup>, both of which have been shown to display n-type conductivity.

### 1.3 Diamond in Electrochemistry

One area which has benefited greatly from CVD of diamond is the electrochemical industry. CVD diamond films are highly desirable in electrochemistry due to diamond's superlative properties, with the following properties providing particular interest:

- BDD possesses a wide working potential window (3 - 4 V) in aqueous and non-aqueous solutions, allowing for an extensive range of solutions to be analysed, which are not possible with alternative electrodes such as platinum, see Fig.1.3.<sup>39</sup>
- The chemical inertness and corrosion resistivity of diamond not only allows for diamond to be used at high temperatures and in chemically harsh conditions, but also in biological and medical environments.
- Diamond's ability to be easily doped in several ways provides access to a tuneable conductivity, ranging from insulator through to conductor, which can be exploited in applications such as semiconductors.
- BDD has a relatively low background current compared to other carbon electrodes. This is due partially to a reduced internal-charge carrier concentration, and also to a smaller pseudocapacitance. The consequence of this is a larger signal/background ratio, and hence a greater sensitivity.<sup>40</sup>
- Diamond shows good resistance to fouling, and can be reactivated by applying an anodic treatment.<sup>41</sup>

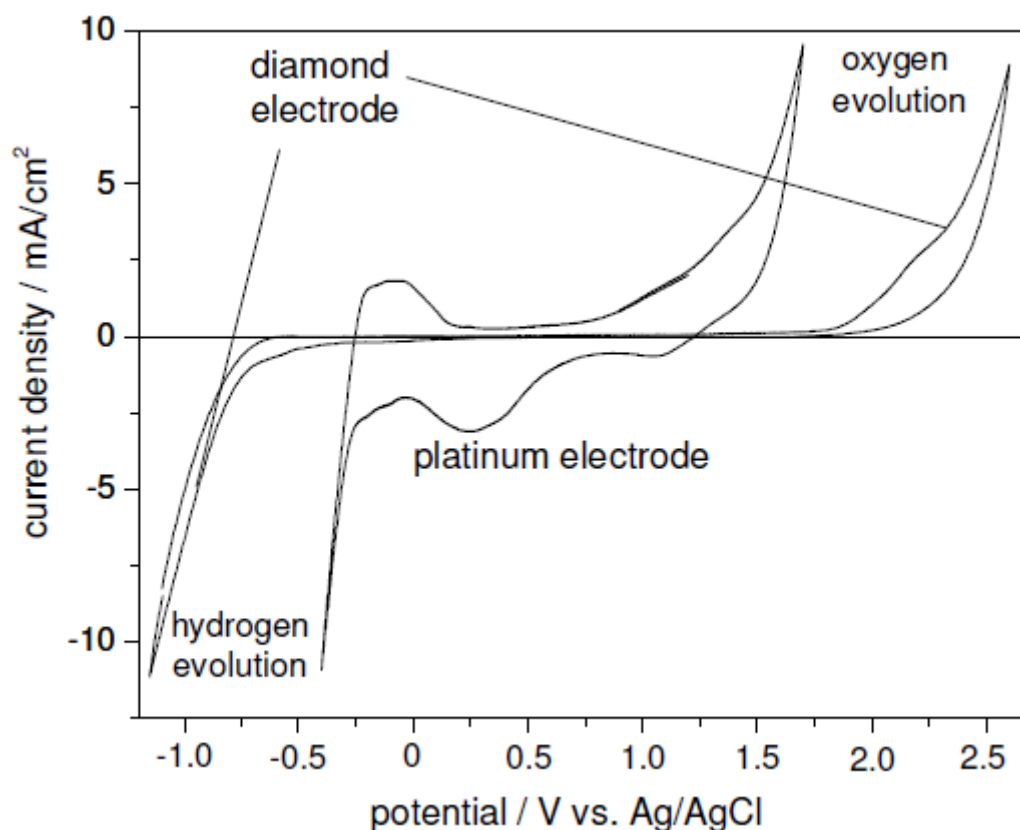


**Figure 1.3.** Cyclic voltammograms ( $100 \text{ mV s}^{-1}$ ) of a diamond and of a platinum electrode in a  $0.2 \text{ M H}_2\text{SO}_4$  solution, highlighting the overpotentials required for oxygen and hydrogen evolution, and thus BDD's wider potential window. Taken from reference 43.

Such properties and their possible combinations, have led to extensive research being carried out into a diverse range of electrochemical applications. In this next section some of the possible electrochemical applications will be explained demonstrating the above properties and the potential benefits available from using synthetic diamond.

### **1.3.1 Boron Doped Diamond Electrodes**

An archetypal application of diamond in electrochemistry is in BDD electrodes. Since their discovery BDD electrodes have, and still are, becoming increasingly popular due to diamond's beneficial properties, mentioned above. These properties make BDD electrodes an exciting alternative to more traditional carbon allotrope electrodes such as glassy carbon, pyrolytic graphite and highly ordered pyrolytic graphite, making many electrochemical applications more attractive and viable.<sup>42</sup> Therefore it is of no surprise that extensive research has gone into exploiting these properties for a variety of applications.

#### **1.3.1.1 Electroanalysis and Sensors**

Diamond's wide potential window and high sensitivity make BDD electrodes exceptional for a wide range of electroanalytical applications, and consequently are already being utilised in several industries. One of the major industries utilising BDD electrodes for electroanalysis is the pharmaceutical industry, which can be used to successfully detect a diverse range of biological molecules including caffeine<sup>43</sup>, glucose<sup>44</sup>, organic acids<sup>45</sup>, serotonin and histamine<sup>46</sup>, purines<sup>47</sup> and even cofactors such as nicotinamide adenine dinucleotide.<sup>48, 49</sup>

#### **1.3.1.2 Water Treatment**

Another series of electrochemical applications utilising BDD electrodes is in chemically harsh environments. Diamond's high resistivity to chemical corrosion allows BDD electrodes to be used in applications such as waste-water treatment, oxidising organic pollutants into carbon dioxide and other biocompatible compounds<sup>50</sup>. BDD electrodes have emerged as the most suitable electrodes<sup>51</sup> for this application, with several other electrode materials being tested, and failing due to surface fouling<sup>52</sup>, limited service life<sup>53</sup>, or selective oxidation<sup>54</sup>.

A second water-treatment application of BDD electrodes is in water purification. BDD's wide potential window in aqueous solutions allows for a variety of strong oxidising

agents to be generated electrochemically for disinfection, removing the need to use chemicals.<sup>55</sup> Not only has this shown to be effective at deactivating a variety of micro-organisms, ranging from bacteria to viruses, but it has also been shown to surpass the efficacy of chlorination, a hugely popular disinfectant process.<sup>11</sup>

Finally, BDD electrodes have also found application in detecting trace amounts of contaminants in water via anodic stripping voltammetry. This includes heavy metal ions commonly found in water such as  $\text{Ag}^+$ ,  $\text{As}^{3+}$ ,  $\text{Cd}^{2+}$ ,  $\text{Cu}^{2+}$ ,  $\text{Pb}^{2+}$  and  $\text{Zn}^{2+}$ , which, even at low concentrations, are known to have dramatic effects on human health and the environment.<sup>56</sup> BDD electrodes are now considered as viable alternatives to mercury-coated glassy carbon electrodes, previously used for water contamination detection. This is due to BDD's wider potential window and lower background current, allowing for a greater range of contaminants, most notably silver (which previously possessed a stripping potential too anodic for detection), to be detected at equally low detection limits.<sup>57, 58, 59, 60, 61, 62, 63</sup>

### 1.3.1.3 Electro-synthesis

BDD electrodes are also being used in electro-synthesis, an area of chemistry which uses electricity to drive the synthesis of organic and inorganic compounds in an electrochemical cell, possessing several advantages such as:

- A reduction/elimination of reactive chemicals involved in a reaction, reducing the hazards associated with the handling and disposal of the reagents, whilst simultaneously decreasing the costs.
- A precise control on the required potential and thus the reaction conditions, allowing for selective transformations and a reduction in toxic effluents.

BDD electrodes, with their high overpotential for oxygen evolution in aqueous electrolytes, makes them well suited for synthesising strong oxidising agents, such as ozone, and they have already been used to electro-synthesise several organic<sup>64, 65</sup> and inorganic<sup>66, 67</sup> compounds. Unlike alternative electrodes, BDD electrodes possess strong resistance to fouling, high chemical corrosion stability and a wide potential window and

therefore overcome the industrial limitations of electro-synthesis, such as electrode stability and performance.<sup>33, 68</sup>

#### 1.3.1.4 Optically Transparent Electrodes

Diamond is optically transparent over a wide wavelength range (225 nm – deep into IR region). Even when doped with boron, diamond remains optically transparent excluding a boron acceptor band and minor two-phonon absorption bands. As a result, BDD electrodes are currently being utilised as optically transparent electrodes (OTE) for spectroelectrochemical measurements. Diamond's short-wavelength cut off (225 nm) extends far below that of conventional OTE electrodes, such as indium and fluorine-doped tin-oxide-coated glass (300 nm), and can therefore be used to provide a greater range of spectroelectrochemical measurements in the UV region.<sup>69</sup>

#### 1.3.1.5 Supercapacitors

A final area of growing interest for diamond in electrochemistry is in double-layer supercapacitors. Diamond's wide potential window provides access to greater operating voltages and thus has attracted a lot of attention recently for applications in energy storage devices, in particular supercapacitors, where the power ( $P$ ) and energy ( $E$ ) density are proportional to the square of the operating voltage ( $V$ ), shown in equations 1.1 and 1.2, where  $C$  and  $R$  represent the capacitance and resistance of the capacitor respectively.<sup>70</sup>

$$E = \frac{1}{2}CV^2 \quad [1.1]$$

$$P = \frac{V^2}{4R} \quad [1.2]$$

BDD supercapacitors have been reported to have a heightened stability over other carbon electrodes, showing relatively small reductions in capacitance over several scans. Unfortunately, the low surface area of these substrates results in a small capacitance with limited applications. Subsequently there have been an increasing number of attempts to increase the surface area of these BDD capacitors by developing nanostructured surfaces. This has been realized through top-down etching<sup>71, 72</sup> and bottom-up growth, both of which are discussed later. Desirable capacitance values are still yet to be observed for BDD supercapacitors but could be realised if larger surface areas were available.<sup>73, 74</sup>

## **1.4 Nanostructured Diamond Electrodes**

Recently a lot of research has gone into developing nano/microstructured diamond films to enhance the inherent properties of diamond for applications such as those mentioned above. One key area of research has been trying to increase the surface area of BDD electrodes. As mentioned previously, an increased surface area would provide a greater capacitance usable for supercapacitors as well as increasing the sensitivity of many electroanalytical techniques discussed, such as waste-water contaminant and drug detection.

In this next chapter, a variety of nanostructured electrodes will be discussed and their electrochemical performance analysed in comparison to flat BDD electrodes. Firstly though, the two most common methods for synthesising nanostructured surfaces, top-down and bottom-up, will be discussed.

### **1.4.1 Top - Down Approach**

By far the more popular of the two methods, the top-down approach involves taking a bulk material and modifying it into the desired shape by etching away unwanted material. This is classically done via plasma etching or reactive ion etching (RIE), shown in Fig 1.4. The top-down technique is well researched and very popular for fabricating integrated circuits and microelectromechanical systems (MEMS), and has begun to be used to fabricate several of the nanostructured electrodes discussed later.

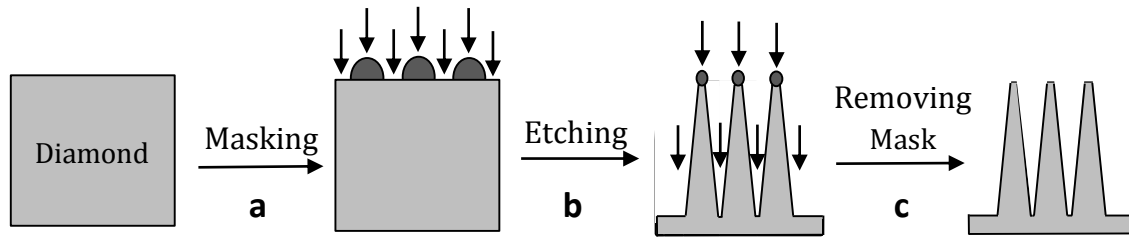


**Figure 1.4.** Schematic diagram of a top-down approach to fabricating a nanostructured surface. Highlighting the following steps **(a)** masking the surface with a protective material **(b)** anisotropic etching of the material **(c)** removing the protective mask.

In the past, diamond's extreme hardness and toughness has meant top – down etching was a difficult process, requiring high temperature molten salts (500 – 700 °C) or an ion beam. Since then however, RIE and plasma etching using O<sub>2</sub>-based gas mixtures have emerged as viable alternatives for etching diamond, possessing good anisotropic behaviour and fine controllability. As a result, a range of diamond nanostructures have been fabricated using the top-down approach, using RIE, and lithographically deposited masking materials to protect the surface. The most common masking materials used in this process are Al, Au, SiO<sub>2</sub>, Mo, Ni or diamond nanoparticles. Other methods have also been used to protect the surface during the etching process, including unintentional oxide impurity sputtering<sup>75</sup>, and deliberate deposition of thin metal films<sup>76</sup>.

#### 1.4.1.1 Nanohoneycomb

Nanohoneycomb diamond structures have been produced from synthetic diamond films using an oxygen plasma and a porous alumina mask, shown in Fig. 1.5. The oxygen plasma selectively etches away the unprotected diamond films resulting in a nanostructure resembling that of honeycomb, shown in Fig. 1.6. As can be seen from the scanning electron microscopy (SEM) images the nanohoneycomb structure is extremely porous with a large surface area, and thus has potential applications as double-layer capacitors, electrodes, optical devices, and even photonic materials.<sup>77, 78, 79</sup>

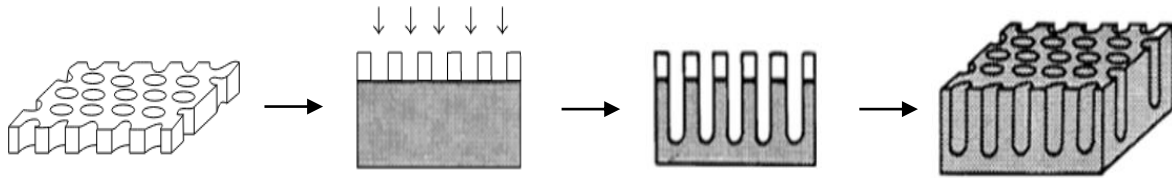


**Figure 1.5.** Schematic diagram of the nanohoneycomb nanostructure fabrication process.

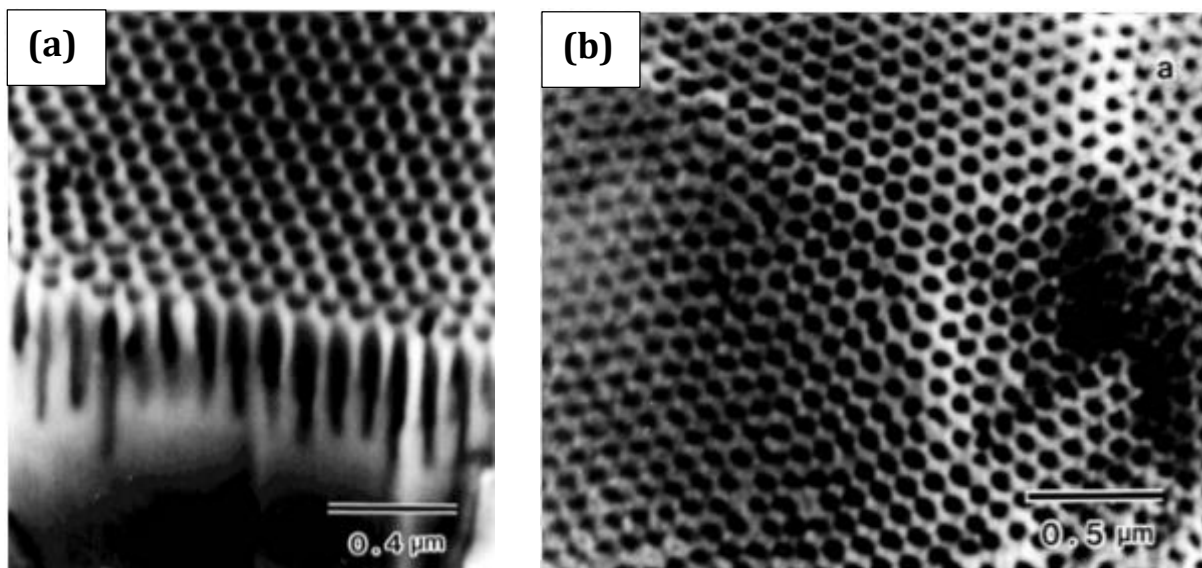


**Figure 1.6.** SEM images of the diamond nanohoneycomb structure displaying a **(a)** cross-section view at a tilted angle of  $45^\circ$  and a **(b)** top down view. Images taken from reference 78.

Nanohoneycomb diamond has been successfully used for electrodes, displaying a capacitance up to 400-fold greater than that of a flat diamond film, which can also be controlled by varying the pore depth and diameter, thus demonstrating how a nanostructure can enhance a diamond film's beneficial properties.

#### 1.4.1.2 Nanowires

Another successful diamond nanostructure fabricated using the top-down approach are diamond nanowires (diameter 8-10 nm), created on boron-doped NCD films using RIE, and seeded diamond nanoparticles as an etching mask. The fabrication process for the nanostructure is shown in Fig. 1.7 and utilized a RIE system consisting of O<sub>2</sub> (97%) and CF<sub>4</sub> (3%). Evident from the atomic force microscopy (AFM) image shown in Fig. 1.8, the effective surface area is increased dramatically compared to a flat diamond electrode, allowing for enhanced electrochemical sensitivities currently utilized for detection of DNA and for other biosensor applications.<sup>79, 80</sup>

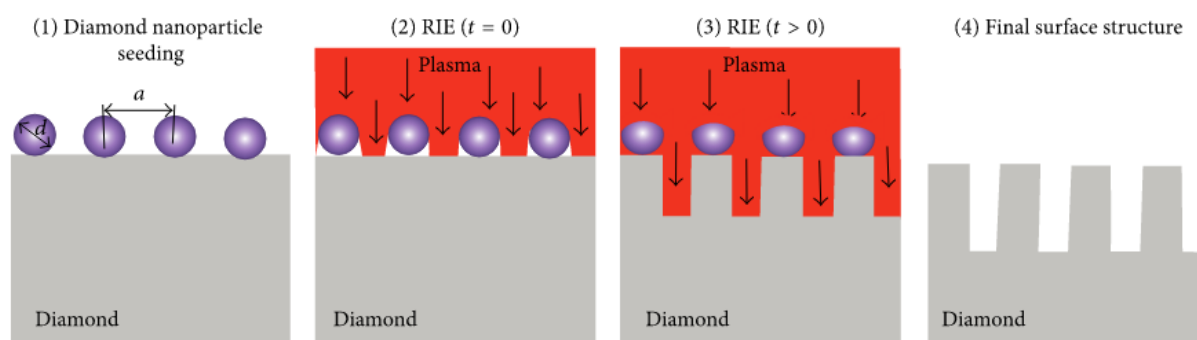


**Figure 1.7.** Schematic diagram of the nanowire nanostructure fabrication process. Image taken from reference 79.

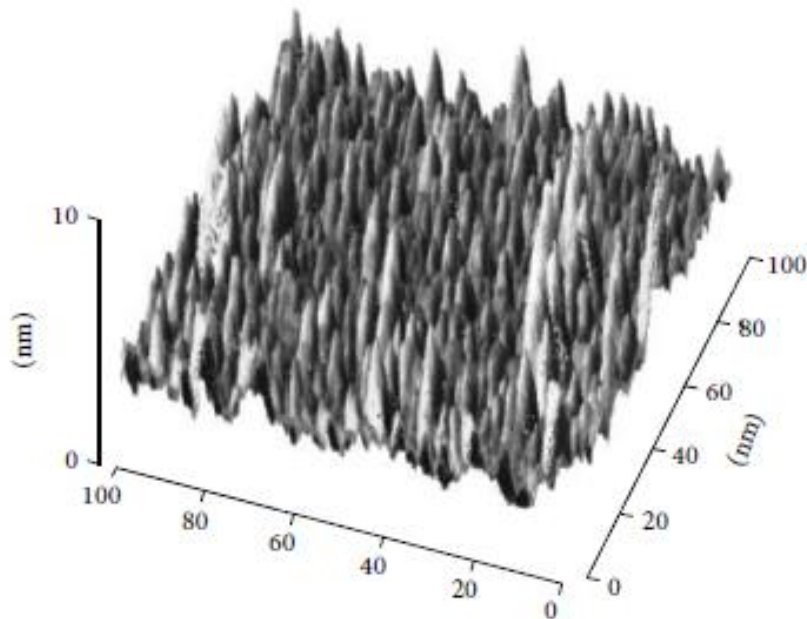


**Figure 1.8.** AFM image of the fabricated nanowire nanostructure. Image taken from reference 79.

#### 1.4.1.3 Nanoneedles

Following the success of nanowires, Lu *et al.* used the same method to develop vertically aligned nanoneedle (diameter  $\sim 10$  nm, length  $\sim 30$  nm) arrays from BDD using the same RIE system ( $O_2$ (97%) and  $CF_4$ (3%)) and etching mask (seeded diamond nanoparticles). The substantial effective surface area of the nanoneedle arrays, coupled with the nanotip effect, resulted in a drastically enhanced gas-sensing ability compared with a flat diamond film. This was demonstrated with ammonia and nitrogen dioxide and suggested nanoneedle arrays could be used preferentially in gas-sensing applications.<sup>79, 81</sup>

More recently Yang *et al.* fabricated larger nanoneedles (diameter  $\sim 70$  nm, length 4-8  $\mu$ m) mask-free using bias assisted RIE with a  $H_2/Ar$  etchant system, shown in Fig. 1.9. Spots of the diamond film were protected from the etchant due to accidental sputtering from the Mo substrate holder, removing the need for an artificial etching mask. This

relatively simple fabrication process recommends nanoneedles for applications in intracellular delivery, electrochemistry, MEMS and field electron emission devices.<sup>82</sup>

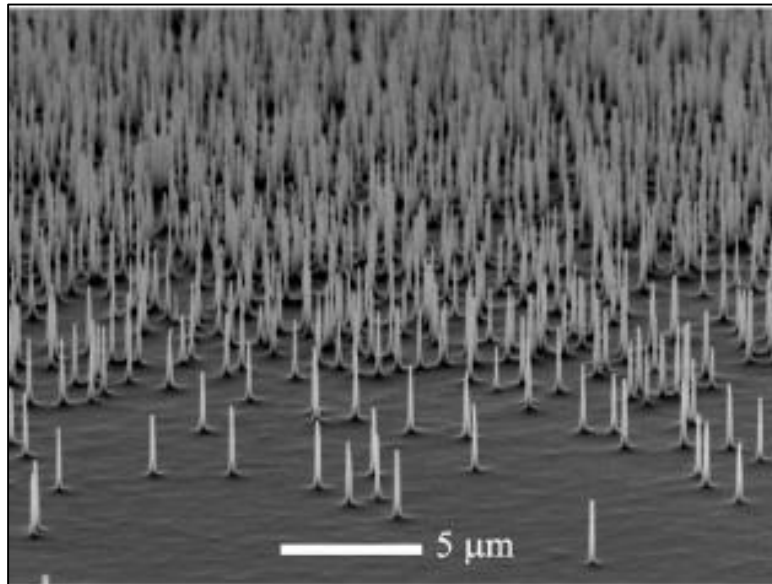


**Figure 1.9.** SEM image of diamond nanoneedles generated using bias assisted RIE and accidental sputtering. Image taken from reference 82.

#### 1.4.1.4 Nanowhiskers

One of the most common diamond nanostructures researched are nanowhiskers (diameter  $\sim 50$  nm, length  $\sim 1\mu\text{m}$ ). It has been shown that diamond nanowhiskers can be produced using a variety of different etchants and masking materials, highlighting the versatility of the top-down method. The favoured etchant for this process has been  $\text{O}_2$  radio frequency plasmas, using Mo or  $\text{Al}_2\text{O}_3$  to mask the surface.<sup>76</sup>

Recently however, it has been shown that by switching to an  $\text{Ar}/\text{O}_2$  etchant, the shape and density of the nanowhiskers can be altered by varying the relative gas concentrations, with a reduction in density seen as the Ar concentration was increased.<sup>83</sup> Another way in which the density of diamond nanowhiskers can be varied is through

metal coatings, shown below in Fig 1.10. Oxidizable metals, for example Mo, have been shown to successfully mask the diamond from etching and hence reduce the density of nanowhiskers. Conversely, non-oxidizable metals, for example Ni, struggle to protect the diamond surface from etching and produce a higher whisker density.<sup>84</sup>

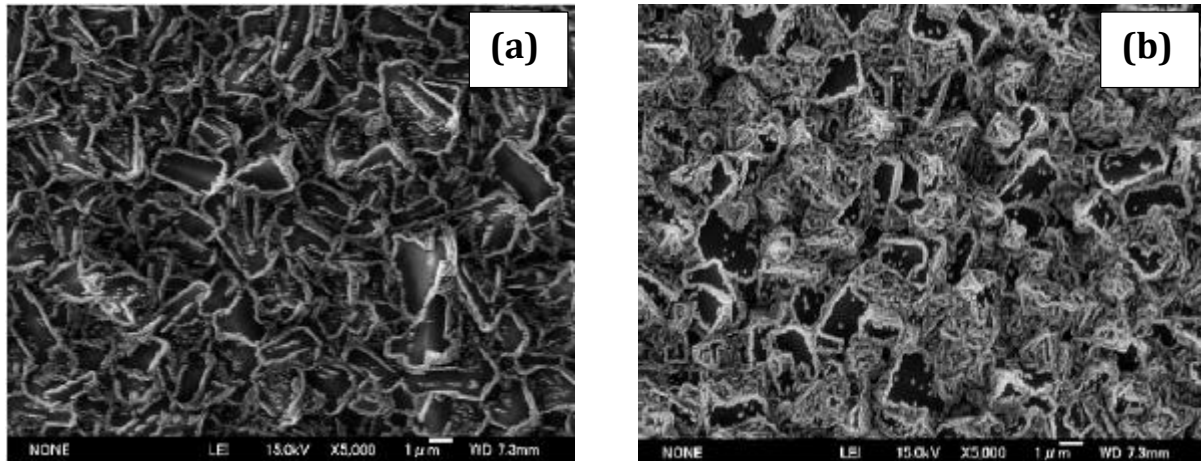


**Figure 1.10.** SEM images of diamond nanowhiskers produced with **(a)** Mo showing a reduced number density and **(b)** Ni showing a larger number density. Images taken from reference 84.

The variability in whisker density gives rise to a range of different applications. Mo-coated diamond nanowhiskers for example have a reduced number density ( $\sim 20 / \mu\text{m}^2$ ), and consequently a high emission current ( $\sim 10^{-5} \text{A} / \mu\text{m}^2$ ), which can be harnessed in field emission devices.<sup>85</sup> Conversely, high density nanowhiskers have been shown to effectively suppress secondary electron emission and consequently are desirable for applications such as electron energy analysers.<sup>86</sup>

## 1.4.2 Bottom-Up Approach

The bottom-up approach is relatively new and far less researched. As the name suggests the process involves building up the surface nanostructure from individual components such as atoms or molecules, and consequently is a lot more time consuming than top-down. For diamond nanostructures this has generally been achieved by overgrowing diamond homoepitaxially, or by coating existing nanostructured substrates such as silicon<sup>87</sup> or CNTs using CVD.<sup>88</sup>

### 1.4.2.1 Vertically Aligned Carbon Nanotube Teepees

Vertically aligned carbon nanotube (VACNT) teepees resemble that of nanowhiskers but are produced using the bottom-up method, and can be grown on top of several substrates (including diamond) via MWCVD and a nickel catalyst. Recently it has been shown that VACNTs can be coated with nanocrystalline BDD and in doing so clump together into bundles resembling ‘teepees’, shown in Fig 1.11. The number of VACNTs incorporated in each ‘teepee’ can range from ~20-100 depending on the number density to begin with. This results in a nanostructured electrode with a heightened surface area, which can be fine-tuned by altering the areal density and length of the VACNTs.

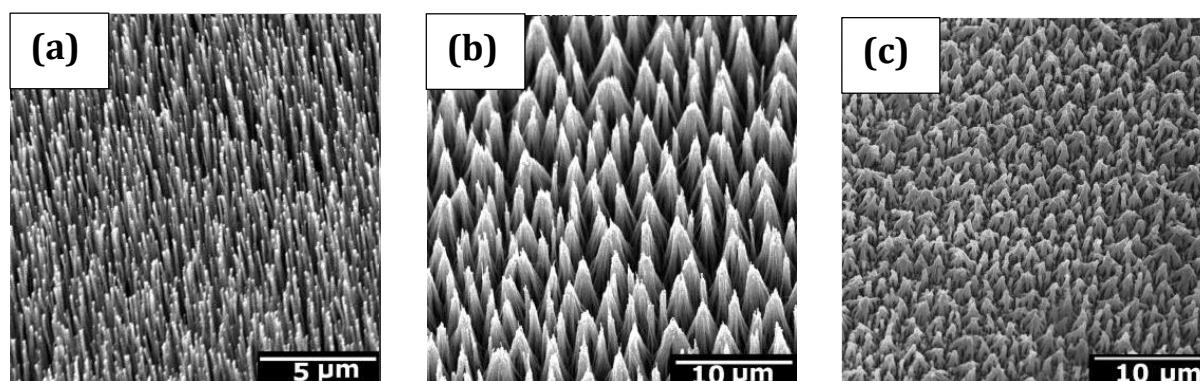


**Figure 1.11.** SEM images of (a) VACNTs, (b) electrospayed VACNTs adopting teepee structures and (c) diamond coated VACNT teepee structures. Images taken from reference 6.

VACNT teepee nanostructures have been successfully shown to increase the surface area and capacitance by up to 450 times when compared to flat BDD electrodes<sup>89</sup>, and are therefore suitable for applications in supercapacitors, bio-sensors, and electroanalysis. VACNT nanostructures can also be exploited in bio-applications such as multielectrode arrays (MEAs) used for neural stimulation and prosthesis. Through the introduction of VACNT teepees, the electrode number and density is increased dramatically, improving the MEAs effectiveness to record electrical activity and deliver electrical microstimulation to neural structures. This enhanced effectiveness makes these MEAs highly desirable for applications in neural prosthesis, neural stimulation, and brain machine interfaces.<sup>90</sup>

#### 1.4.2.2 Nanorod Forests

Diamond nanorod forests are an interesting nanostructure that utilizes both top-down and bottom-up techniques in their fabrication, shown in Fig 1.12. Similarly to VACNTs, diamond nanorod forests are fabricated by CVD of BDD onto a high-surface-area substrate, silicon nanowires. The two processes differ greatly, though, in how the high-surface-area substrate is generated. Unlike VACNTs, which are grown onto a substrate, silicon nanowires are formed through electroless metal deposition (EMD). This process results in the silicon substrate being etched away leaving silicon nanowires ready for CVD.<sup>91</sup>

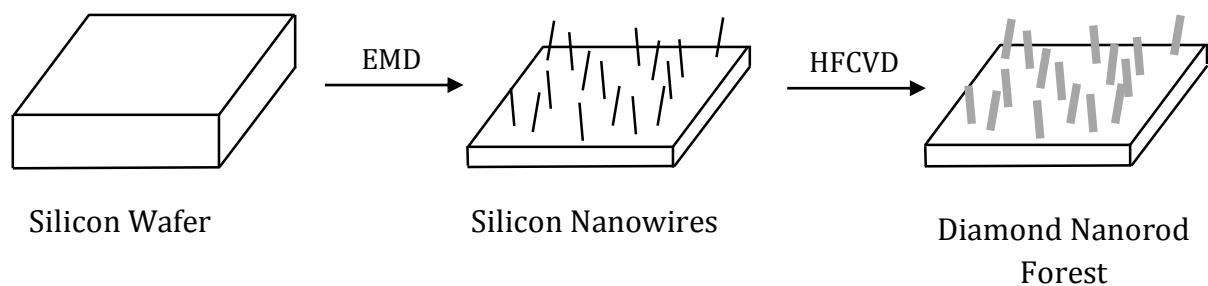


**Figure 1.12.** Schematic diagram for the fabrication of diamond nanorod forest electrodes. Highlighting the formation of silicon nanowires via EMD before diamond coating using HFCVD.<sup>87</sup>

Once generated the silicon nanorods are coated with a diamond film typically using HFCVD, resulting in a high surface area BDD electrode, shown in Fig. 1.13. Similarly to nanowires discussed previously, the tips of the diamond nanoforests can be electrochemically functionalised and consequently have been targeted for applications in biochemistry, in particular, as a nonenzymatic glucose sensor. Promising results have subsequently emerged regarding this application, showing high electrochemical activity towards glucose oxidation, good selectivity, and good stability.<sup>87, 92</sup>

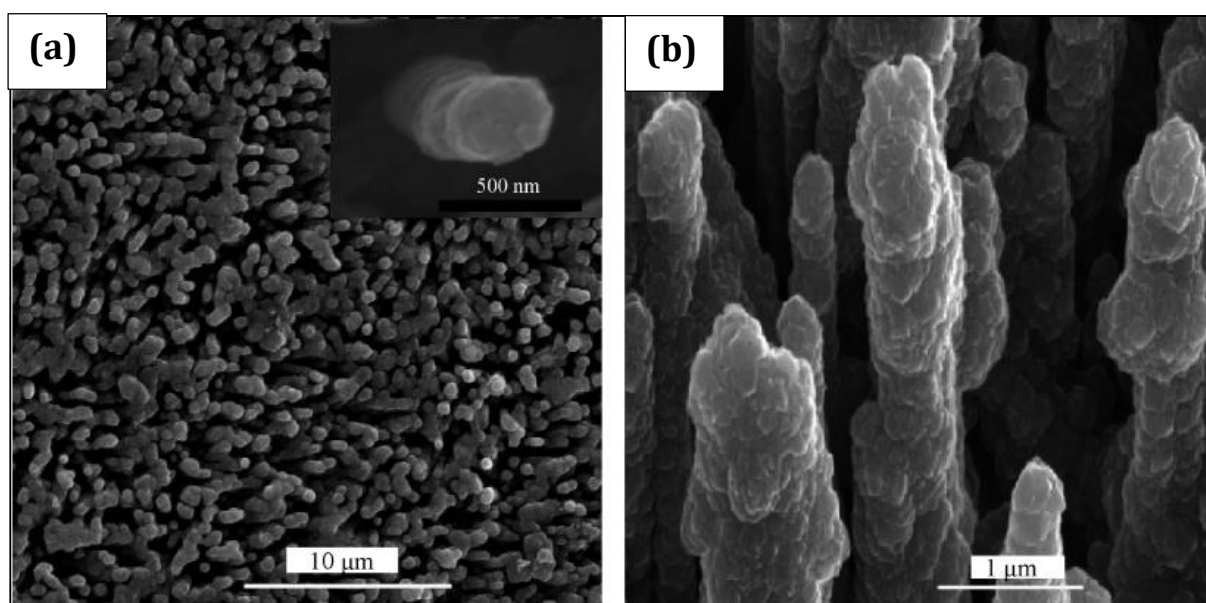


**Figure 1.13.** SEM images recorded of a diamond nanoforest electrode from **(a)** top and **(b)** side view. Magnified image of a single diamond nanowire is shown in the inset of **(a)**. Images taken from reference 87.

### 1.4.2.3 Umbrella Structures

A less well known bottom-up diamond microstructure is diamond umbrellas. The umbrella structures are fabricated by anisotropic growth through holes present in a titanium mask. Once the diamond surface is level with that of the titanium mask, shown in Fig 1.14, the diamond begins to also grow laterally, resulting in the umbrella microstructure shown in Fig. 1.15. The umbrella structure is achieved by controlling the growth rates ( $v_{001}$  and  $v_{111}$ ) of particular diamond faces and using an  $\alpha$  parameter, defined below, of approximately 3.

$$\alpha = \sqrt{3} \frac{v_{001}}{v_{111}}$$

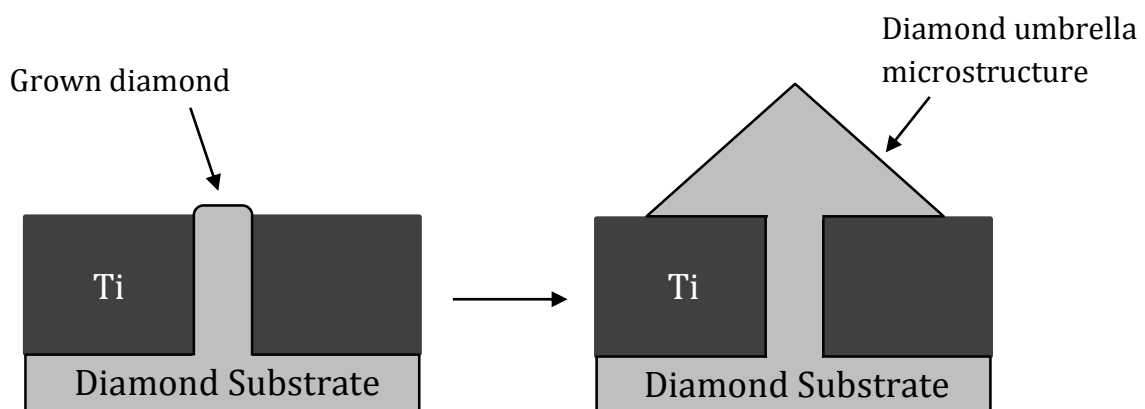


**Figure 1.14.** Schematic diagram for the growth of diamond microstructured umbrellas, highlighting the diamond's growth through holes in a titanium mask before lateral growth.

Although this nanostructure doesn't maximise the possible surface area of diamond, it does demonstrate the benefits of specific nanostructures, resulting in an increased photon collection efficiency compared to bulk diamond and nano-rod structures. Consequently diamond umbrellas are ideal for magnetic sensors used in quantum computing and biological observations.<sup>93</sup>

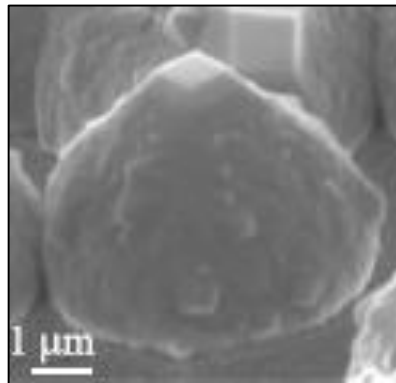


**Figure 1.15.** SEM images of an individual diamond umbrella microstructure.

## 1.5 Antibacterial Nanostructured Surfaces

As demonstrated by the umbrella nanostructure, diamond nanostructures have many advantages besides just increasing the surface area of electrodes. This even extends beyond electrochemistry as a whole, with recent research indicating that nanostructures can effectively kill bacteria cells.

E. Ivanova *et al.* discovered that a cicada's (*Psaltoda claripennis*) ability to effectively kill the human pathogen *Pseudomonas aeruginosa* was due to the nanostructured surface of the insect's wings. This bactericidal property was also displayed by the wings of dragonflies (*Diplacodes bipunctata*) and by black silicon needles, a nanostructure closely resembling the pillared surface of the dragonfly wings. Furthermore, gold nanostructures, including gold-coated cicada wings, have also been shown to be equally

effective, confirming the physical structures responsibility for bactericidal properties.<sup>94, 95, 96</sup>

Consequently a new area of research has been established, designing nanostructured surfaces to effectively kill bacteria using only the physical properties of the surface. One area of interest is in diamond nanostructures, which would provide a greater longevity and chemical inertness not possible with current nanostructures, providing extended lifetimes of existing applications and access to new applications, such as prosthetic coatings.

## **1.6 Project Objectives**

The principal objective of the project was to use HFCVD to fabricate a variety of BDD electrodes using a bottom-up approach, with an enhanced sensitivity, due to a large surface area. This was realized by coating high-surface-area substrates in a variety of different diamond films, varying in crystallinity and thickness. These electrodes were then analysed electrochemically to confirm their enhanced sensitivity and optimise the deposition conditions required. The motivation behind this objective was that the electrode's enhanced degree of sensitivity could eventually be applied to existing electrochemical applications, such as waste-water anodic stripping voltammetry and pharmaceutical drug detection, allowing for lower concentrations of molecules to be detected. The four nanostructures investigated were:

1. Small black silicon needles
2. Large black silicon needles
3. CNT webs
4. CNT teepees

A second objective was to fabricate a nanostructured diamond surface with bactericidal properties, for potential applications as hospital handrail and door handle coatings. This objective focussed primarily on the black silicon needles nanostructures.

## 2. Experimental

---

### 2.1 Electrode Fabrication

The nanostructured electrodes were produced via a bottom-up approach, using HFCVD to deposit a diamond film onto existing nanostructured substrates.

#### 2.1.1 Substrate Preparation

The two substrates utilized were black silicon needles and CNTs and were prepared in the following ways.

##### 2.1.1.1 Black Silicon Needles Substrates

Two wafers of black silicon needles were supplied by Colin Welch of Oxford Instruments. Each was produced by RIE of a silicon substrate. A  $\text{Cl}_2\text{-O}_2$  plasma was used to simultaneously deposit micromasks and anisotropically etch the silicon surface, resulting in a wafer of short needles ( $\sim 1\ \mu\text{m}$  in length) and a wafer of pointy large needles ( $\sim 5\ \mu\text{m}$  in length), shown later in Fig 3.1 and 3.2 respectively.

Using a diamond scribe and tweezers,  $1\ \text{cm}^2$  samples were produced by fracturing the large wafer down grain boundaries. These  $1\ \text{cm}^2$  samples went on to form the substrates for CVD and ultimately the electrodes.

##### 2.1.1.2 CNT Substrates

VACNT forests and CNT webs were grown on  $1\ \text{cm}^2$  silicon substrates using a nickel catalyst and a plasma enhanced CVD reactor, via the method outlined by Zou *et al.*<sup>6</sup>

#### 2.1.2 Electrospray Seeding

Once fabricated, the black Si and CNT substrates were then electrosprayed (35 kV) with a detonation nanodiamond/methanol solution (10 drops of detonation nanodiamond dispersed in water 2.0 w/v % in  $\sim 25\ \text{mL}$  methanol), sonicated for 30 mins before use. In doing so the substrates became seeded with nanodiamond crystals, thus increasing the nucleation density and increasing the diamond growth rate. This was performed using the apparatus displayed in Fig. 2.1.

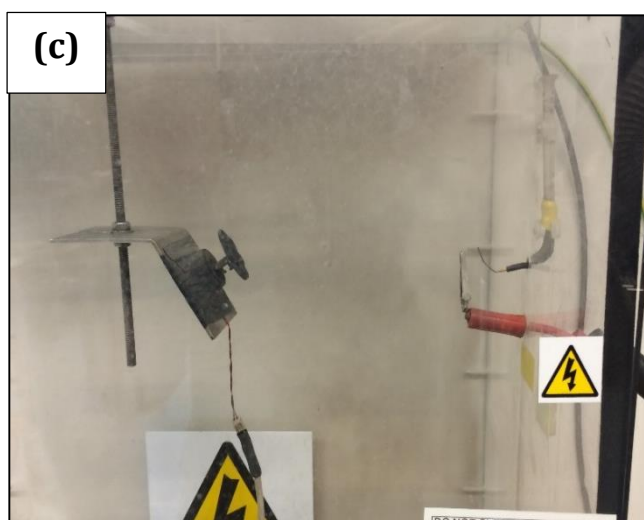
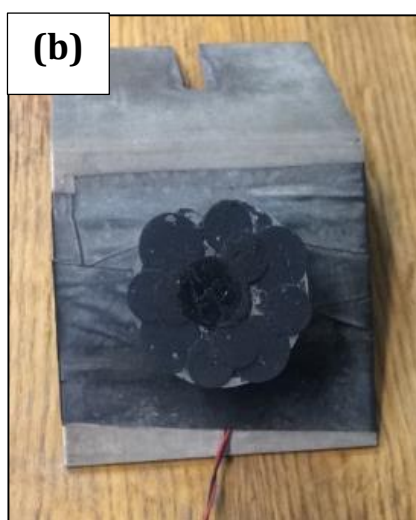
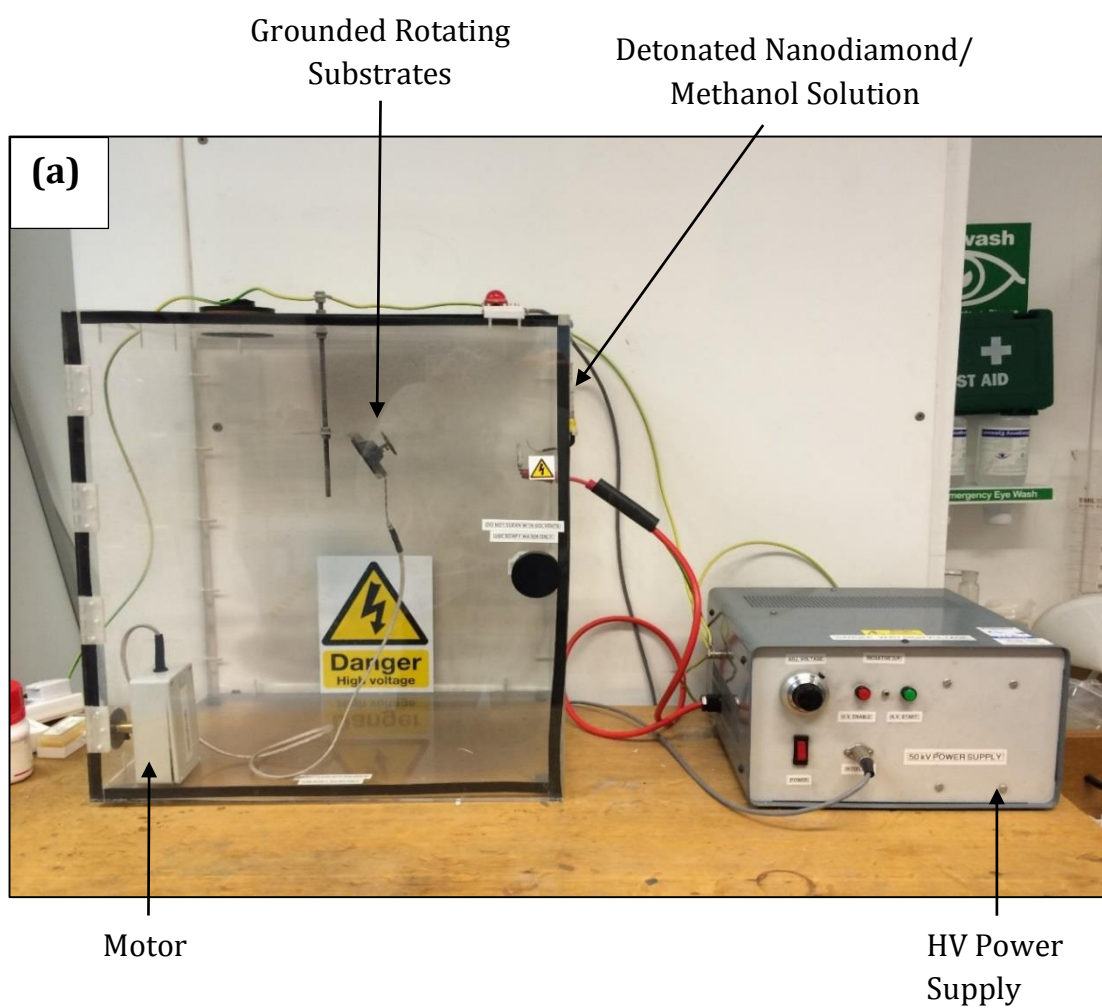


**Figure 2.1.** (a) Electro spray apparatus used to seed substrates with nanodiamond highlighting (b) the substrate holder and (c) the electro spray pathway.

The electrospray procedure is as follows and is also outlined in Fig.2.2. The substrates are first secured to a grounded rotating disc using carbon adhesive pads. Once secure the disc begins spinning ( $\sim 60$  rpm is optimal), powered by an electric motor, ensuring a uniform seeding of nanodiamond. The HV power supply is then connected to the syringe needle and the detonated nanodiamond suspension added. Finally the power supply is turned on applying a high voltage to the tip of the syringe, ionizing the diamond solution creating an aerosol which is attracted towards the grounded substrates.

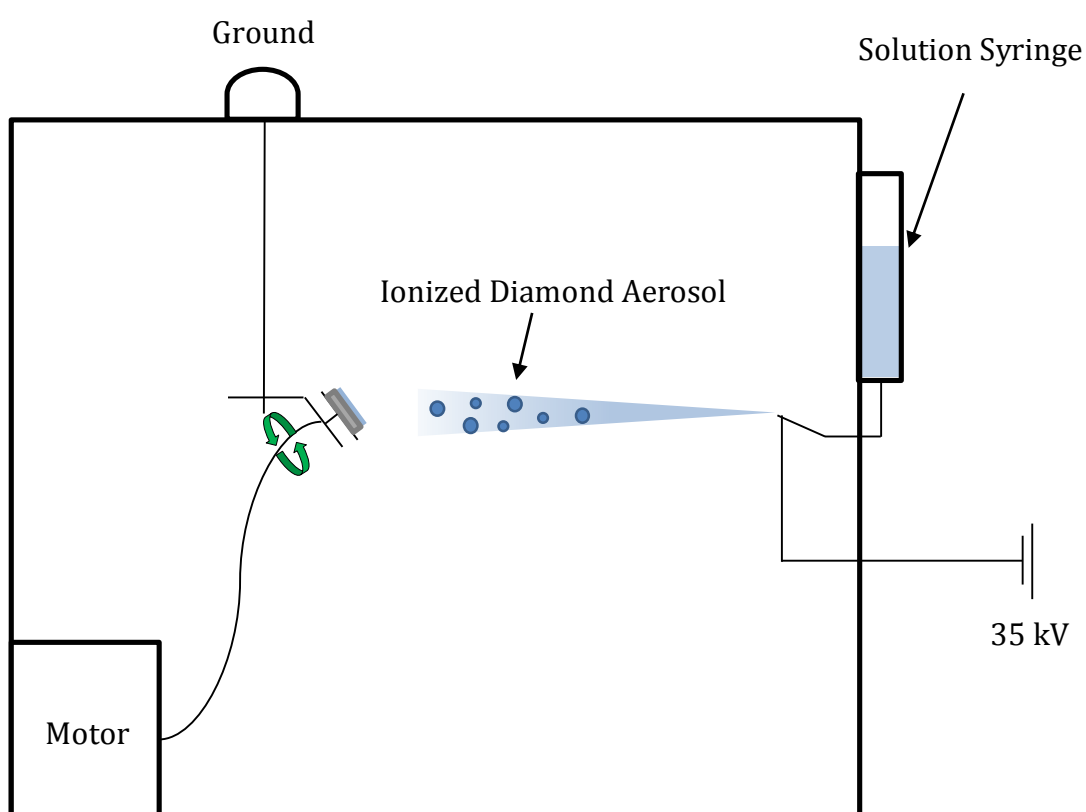


**Figure 2.2.** Schematic diagram showing the formation of the ionized diamond aerosol and its attraction towards the grounded substrate.

### 2.1.3 Depositing a Diamond Film

The seeded substrates were then coated in a BDD film, all of which were deposited using HFCVD, the apparatus of which is pictured in Fig. 2.3 & 2.4. For MCD films flow rates of 200, 2 and ~450 sccm were utilized for hydrogen, methane and diborane respectively. The flow rate of methane was increased to 5 sccm when NCD films were desired. All depositions were performed at ~20 Torr and ~1000 K, controlled by applying a 25 A current through the tantalum filaments. The deposition time ranged from 15 minutes – 3 hours depending on the desired thickness of the diamond film, and are summarised in Chapter 3.1.

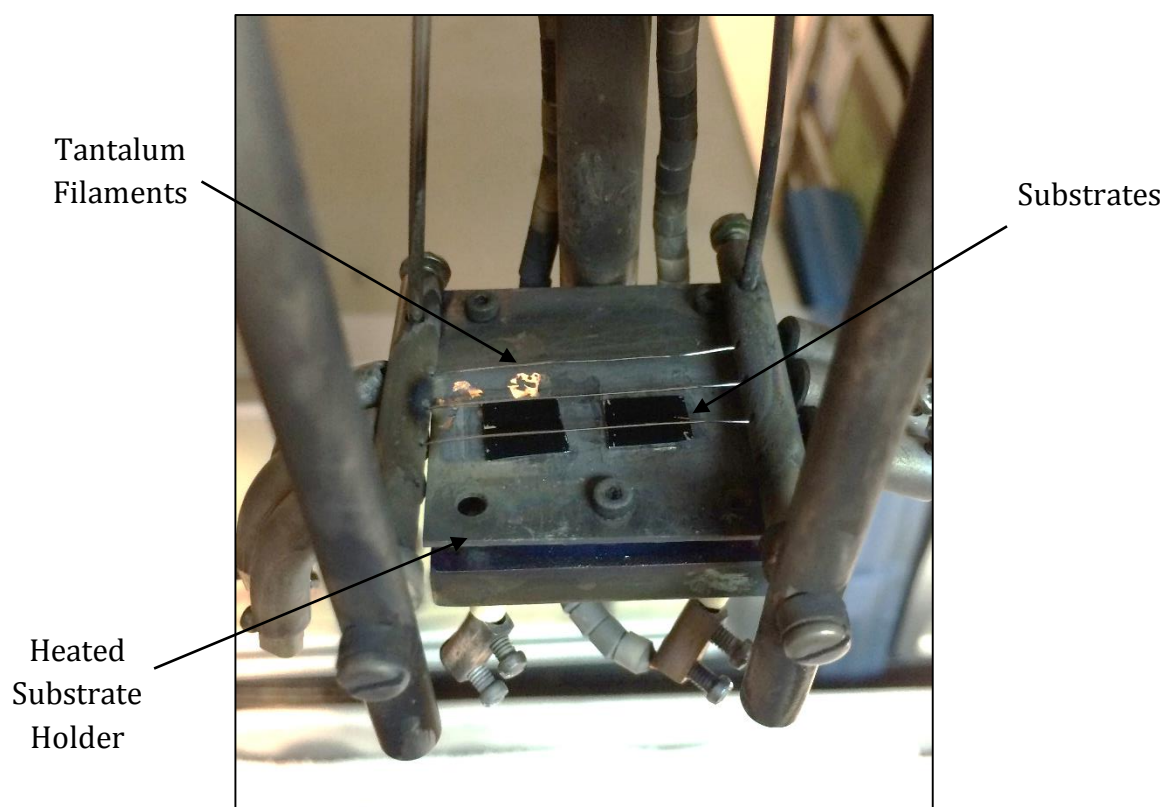


**Figure 2.3.** Annotated photo of the substrate holder used in the HFCVD reactor.

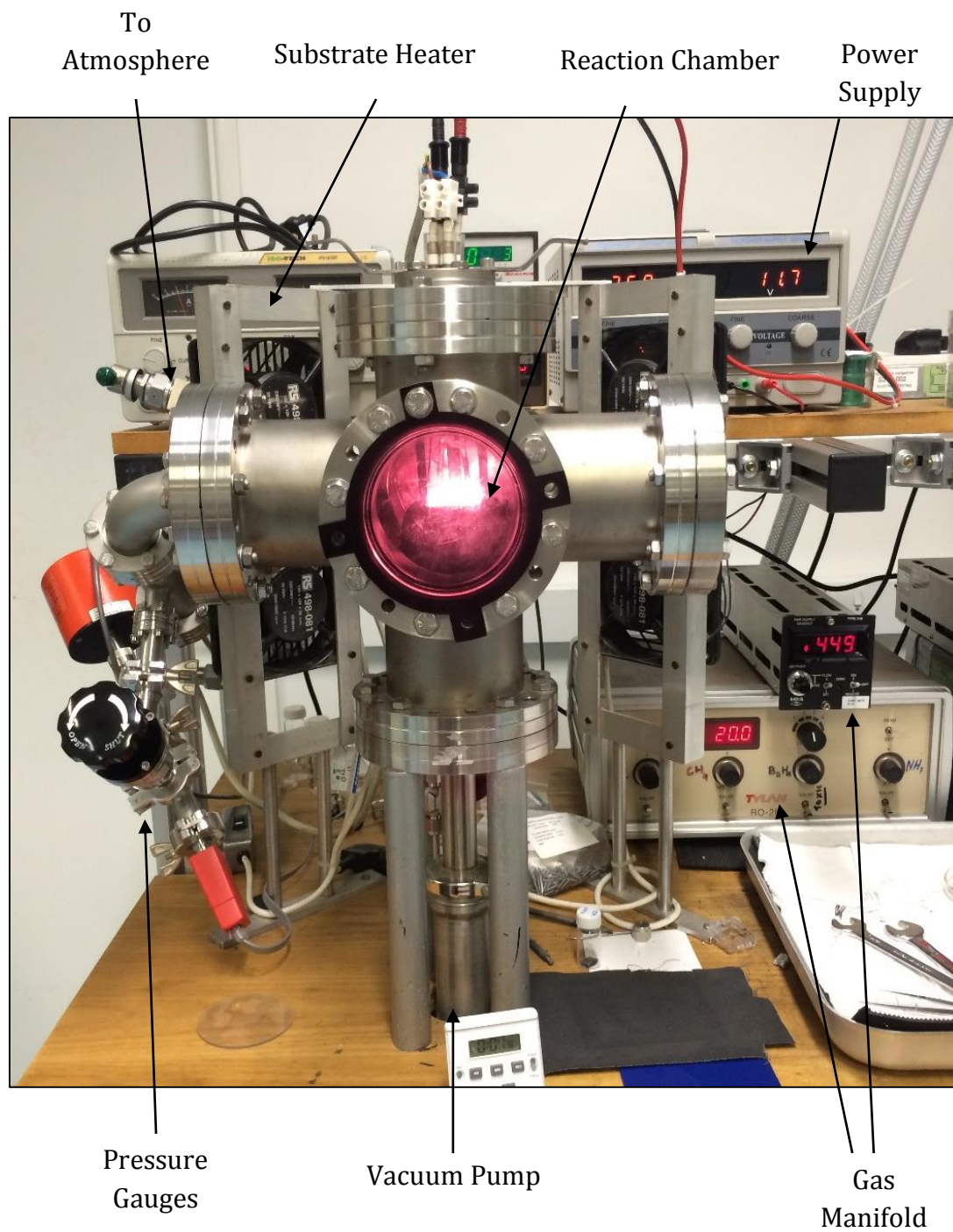


**Figure 2.4.** Annotated photo of the reactor used for HFCVD.

## 2.2 Anti-Bacterial Surfaces Fabrication

Initial 1 cm<sup>2</sup> substrates were prepared from a large black silicon wafer identically to those prepared for the electrodes discussed previously. HFCVD was then used, as discussed earlier, to grow diamond films on the unseeded substrates of various crystallinity and thickness, summarised in chapter 3.1. Once grown the samples were cut into quarters (~0.25 cm<sup>2</sup>) using a laser cutter. This was repeated until ten 0.25cm<sup>2</sup> substrates of each sample were created. The diamond samples were then acid washed in concentrated sulfuric acid (>95%, 10mL, 80 °C) for 30 minutes and hydrogen terminated using a HFCVD reactor.

## 2.3 Antibacterial Surface Testing

These samples were then supplied to Dr Gavin Hazell in the School of Oral and Dental Sciences who performed the following experiments to determine if they acted as an antibacterial surface. Each sample was rinsed with absolute-ethanol before being submerged in 2 mL of a *Pseudomonas aeruginosa* bacterial suspension. The samples were then incubated for 1 hour at 37 °C before being rinsed with Tris-HCl buffer to remove any non-adherent bacteria. 1 mL of Live/Dead® BacLight™ bacterial viability stain was then applied to each surface followed by incubation at 25 °C for 15 mins, and a final rinse using Tris-HCl buffer. The prepared samples were then maintained in 1 mL of Tris-HCl buffer whilst fluorescence microscopy was used to visualise the bacterial viability. Finally *Image J* Software was then used to quantify the number of bacteria cells with an intact cell membrane (viable) and a damaged cell membrane (dead).

## 2.4 Electrochemical Analysis

The various electrodes were analysed electrochemically via cyclic voltammetry using two solutions, a potassium nitrate solution (0.1 M, 5 mmol, 5.055 g) and a potassium ferricyanide (1 mM, 0.25 mmol, 0.0823 g) with potassium nitrate (0.1 M, 5 mmol, 5.055 g) supporting electrolyte solution. The electrolyte solution (75 mL) was placed into a glass beaker along with the diamond working electrode, a Ag/AgCl reference electrode, and a Pt counter electrode. Cyclic voltammograms (CVs) were then recorded between the following potential ranges -0.1 to +0.5 V and -0.1 to +0.1 V using the following scan rates,

5, 10, 20, 25, 40, 50, 60, 75, 80, 100 and 200 mV/s. A conditioning step was applied before every scan which entailed applying the starting voltage for 120 s followed by a 10 s equilibration. This was performed using *General Purpose Electrochemical System (GPES) version 4.9.007* software and a Fra 2 Autolab Type III potentiostat.

The apparatus shown in Fig. 2.5 was utilized to form the working electrode, allowing the geometrical surface area of the electrode to be fixed, and the sample undamaged. When closed, the plastic block forces the BDD substrate down onto the O-ring and copper tape, forming a connection and exposing a defined area of the substrate to the electrolyte solution.

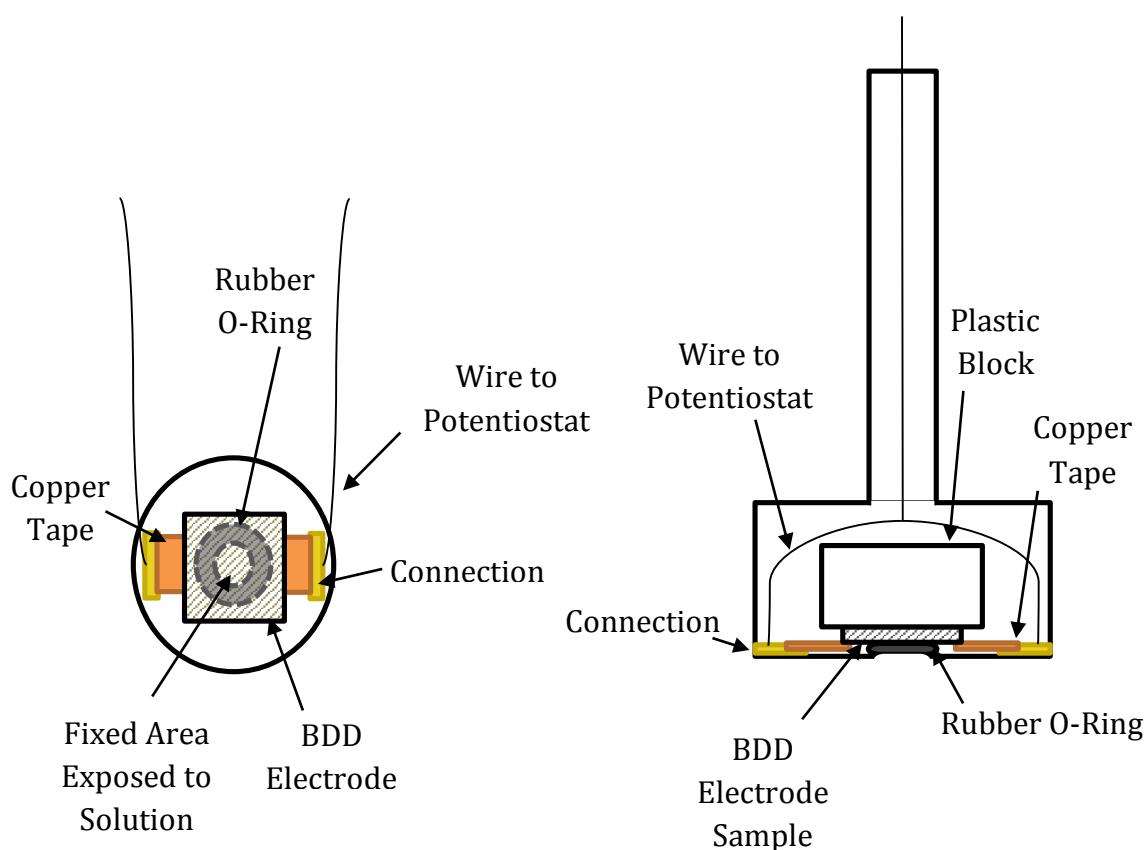


**Figure 2.5.** Top down and side on diagrams for the working electrode apparatus used.

A second method was also used to control the geometric area of the electrodes when testing them electrochemically, shown in Fig. 2.6, and involved using Teflon tape, conductive silver paint, and copper tape. Teflon tape with a  $7 \text{ mm}^2$  hole was placed on top of the electrode leaving part of the electrode surface exposed to form a connection. Conductive silver paint was applied to this region and copper tape applied on top before finally being covered in Teflon tape. This provided a greater connection to the electrodes and was therefore utilised for the electrochemical measurements reported.

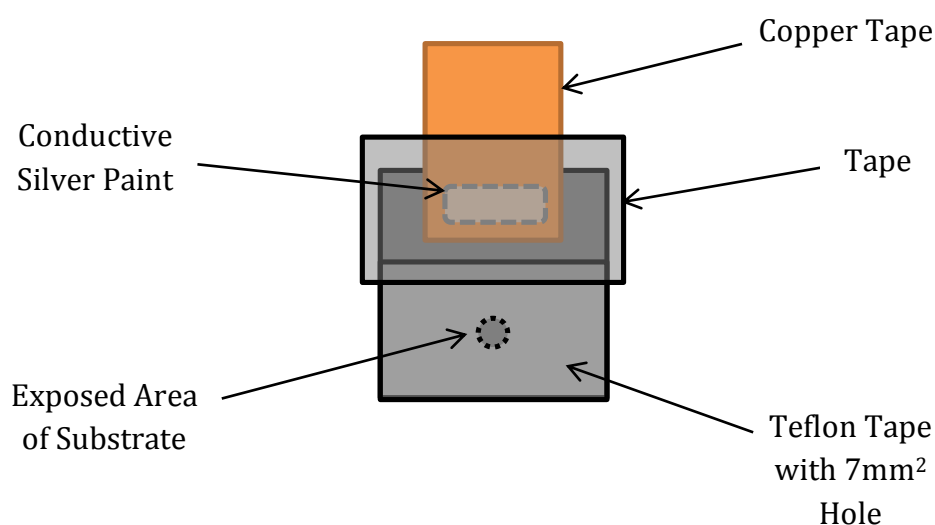


**Figure 2.6.** Diagram of the apparatus used for the working electrode.

## 2.5 Electrochemical Impedance Spectroscopy

Electrochemical impedance spectroscopy (EIS) measurements were recorded over the frequency range  $0.1 - 3000 \text{ Hz}$  at  $0.221 \text{ V}$ , using a frequency response analyser. These measurements were performed utilizing the same electrochemical set up and potassium ferricyanide solution discussed earlier.

## 3. Results and Discussion

---

### 3.1 Diamond Films

As mentioned previously, a range of diamond films, varying in crystalline size and thickness, were deposited on to the substrates by altering the deposition conditions. The range of films deposited is summarised in table 3.1. As can be seen, the large black silicon needles nanostructure was the focus of much of the work. This was partially due to limited availability of CNT substrates but also as it appeared to have the highest surface area.

**Table 3.1.** Summary of films deposited onto the various substrates.

<b>Substrate</b>	<b>Diamond Film Crystallinity</b>	<b>Deposition time / min</b>
Large Black Silicon Needles	MCD	20
		30
		45
		60
		75
		90
		105
		120
		180
Large Black Silicon Needles	NCD	15
		20
		30
		40
		60
		80
		100
		120

		180
		210
		240
Small Black Silicon	MCD	30
Needles		45
		60
		90
		120
	NCD	60
		90
CNT Webs	MCD	20
		30
		45
	NCD	60
VACNT Teepees	MCD	20
		45
	NCD	60

### 3.1.1 Scanning Electron Microscopy

The first analytical technique used to analyse the diamond films was SEM. SEM was used to provide clear images of the substrates before and after deposition of the diamond films, and was used to confirm the coating of the nanostructures in a diamond film.

#### 3.1.1.1 Small Black Silicon Needles

Unlike the larger needles, discussed later, the seeded small black silicon needles substrates were completely overgrown by diamond even at times as short as 30 minutes. In order to solve this problem the substrates were not seeded for the following depositions, lowering the initial growth rate and allowing for the nanostructure to be maintained. Due to the reduced growth rate the deposition times were extended to ensure a complete coating, which was achieved after 1 hour 30 minutes, shown in Fig 3.1. Depositions longer than this (up to 2 hours) showed similar results, with shorter depositions resulting in incomplete coating or only coating the tips of the needles.

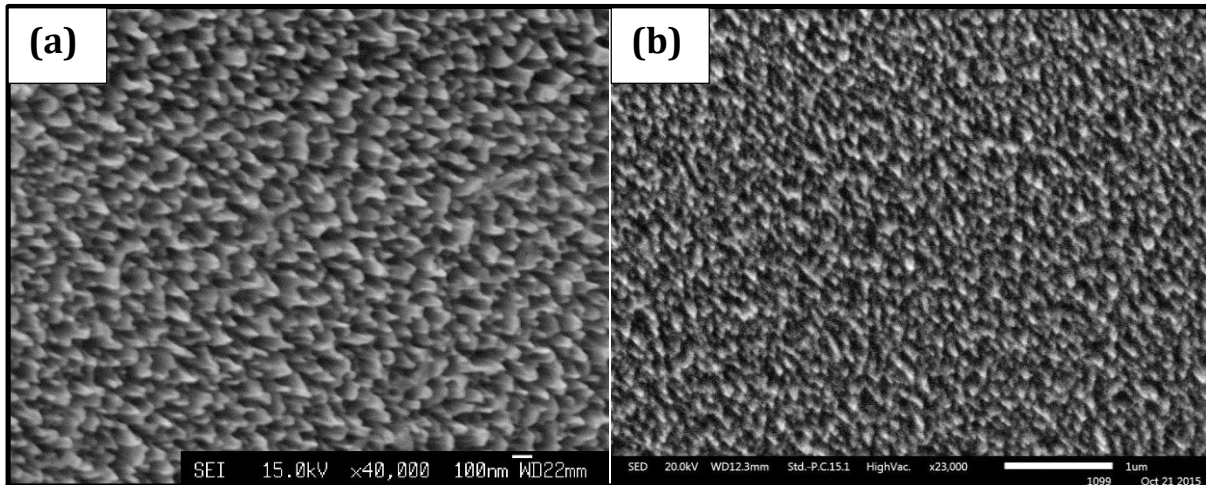


**Figure 3.1.** SEM images of the small silicon needles **(a)** uncoated and **(b)** coated in MCD.

### 3.1.1.2 Large Black Silicon Needles

When seeded, the large black silicon needles substrates were shown to be successfully coated in MCD, shown in Fig. 3.2, all the way down to the base of the needle, after 30 minutes of deposition. Subsequent deposition runs showed that the deposition time could be reduced to as short as 20 minutes with the nanostructure remaining fully coated. NCD's faster growth rate meant that complete coatings could be achieved at even shorter deposition times of 15 minutes.

Longer deposition times were then performed to investigate the effect of diamond thickness on the nanostructure. The diamond films produced appeared to show a reduction in needle height and a broadening of needle shown in Fig.3.3. Finally extremely long deposition times were executed (up to and including 4 hours) to completely overgrow the nanostructure, expecting a typical flat diamond film to be formed. Instead a porous structured NCD film resulted with short needles coalescing towards the tips, shown in Fig 3.4, and was treated as a separate nanostructure for the subsequent analysis.

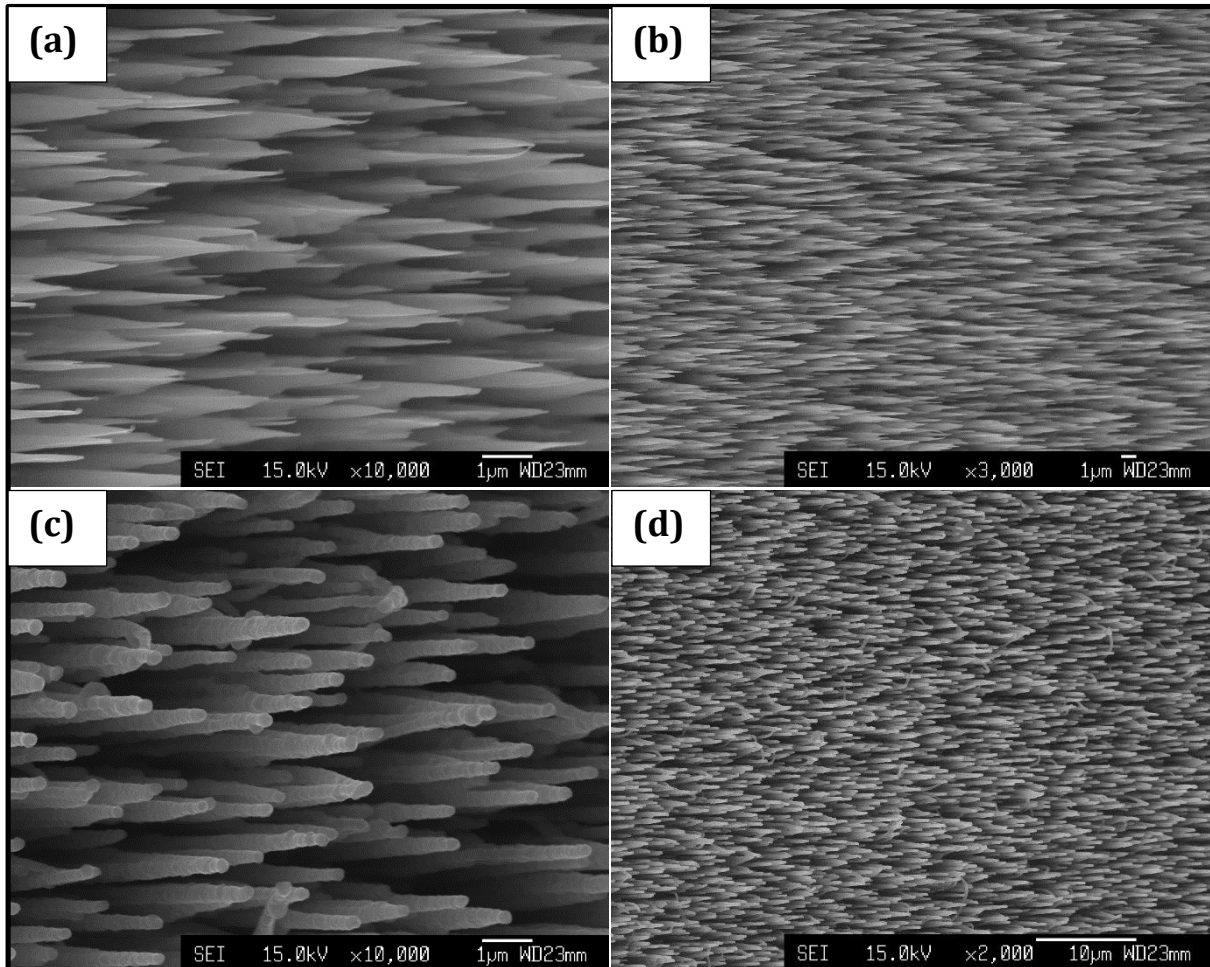


**Figure 3.2.** SEM images for large silicon needles **(a)** & **(b)** uncoated, and **(c)** & **(d)** coated in MCD.

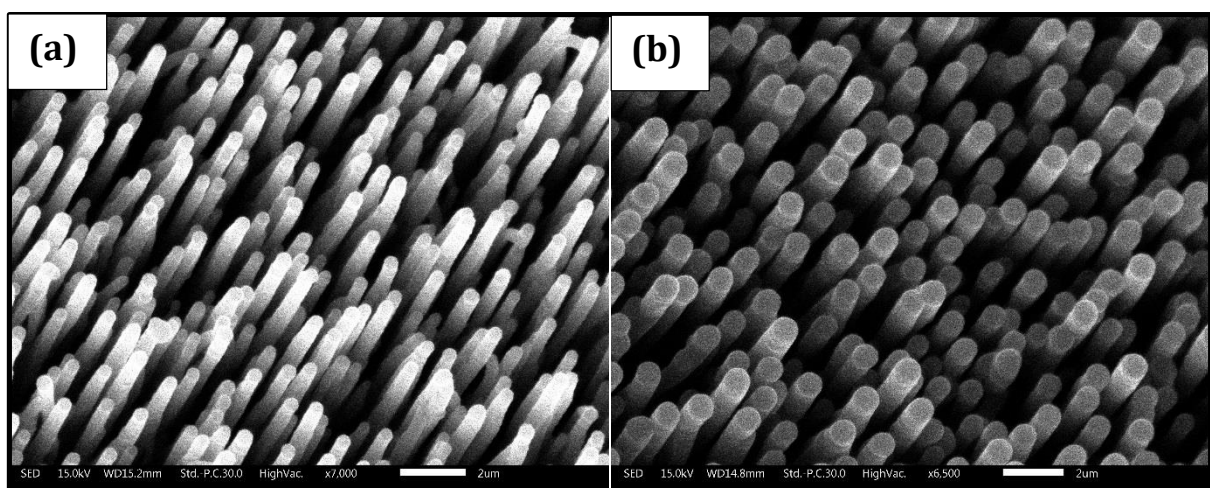


**Figure 3.3.** SEM images of NCD films grown for **(a)** 40 mins and **(b)** 80 mins, highlighting tip broadening associated with prolonged depositions.

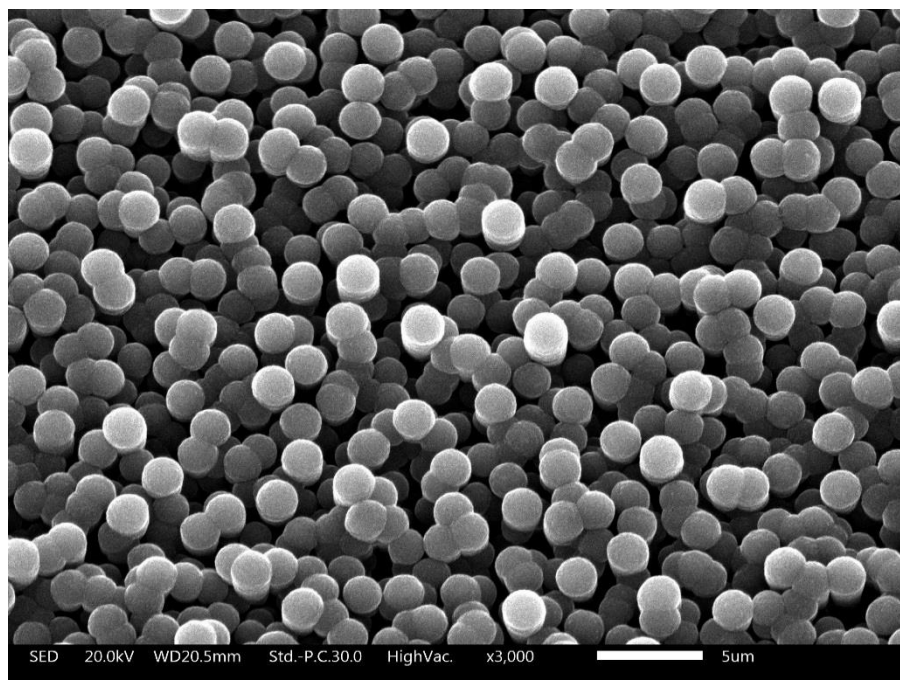


**Figure 3.4.** SEM image of the nanostructured surface after prolonged deposition of NCD (3 hours).

### 3.1.1.3 CNT Webs

The CNT web nanostructure, shown in Fig 3.5, was shown to be fully coated in MCD and NCD films at deposition times of 20 and 45 mins, respectively, but shorter deposition times were likely possible.

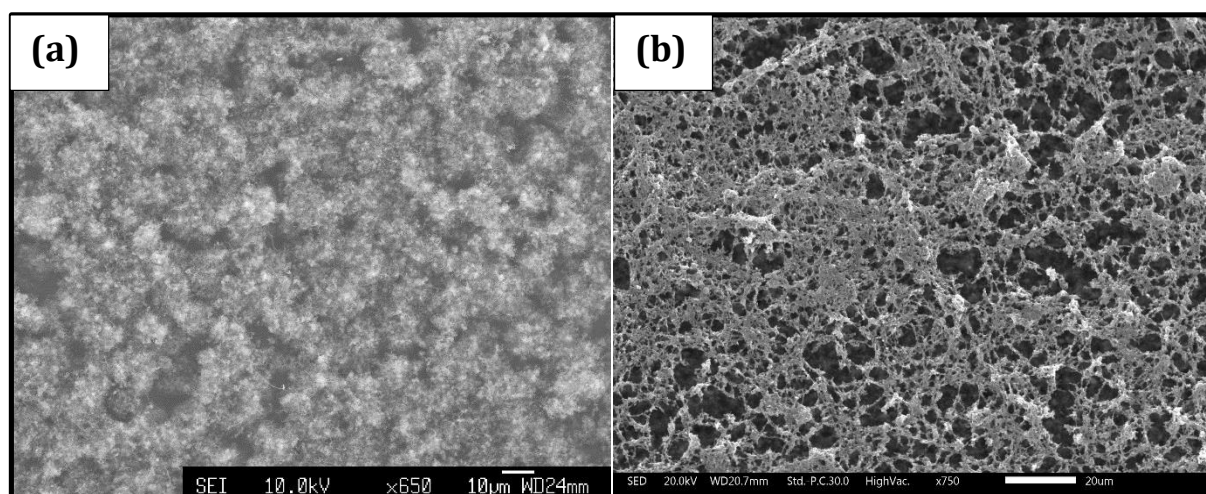


**Figure 3.5.** SEM images of (a) uncoated CNTs and (b) coated in MCD.

### 3.1.1.4 VACNT Teepees

As shown below in Fig 3.6, upon wetting the VACNTs using electrospray, the VACNTs clumped together to form teepee structures. As with the other CNT nanostructure, deposition times of 20 and 45 mins were recorded for complete coatings of MCD and NCD respectively, although shorter times are likely possible. Prolonged deposition of MCD was investigated and showed a greater coalescence of CNT and a reduction in surface area.

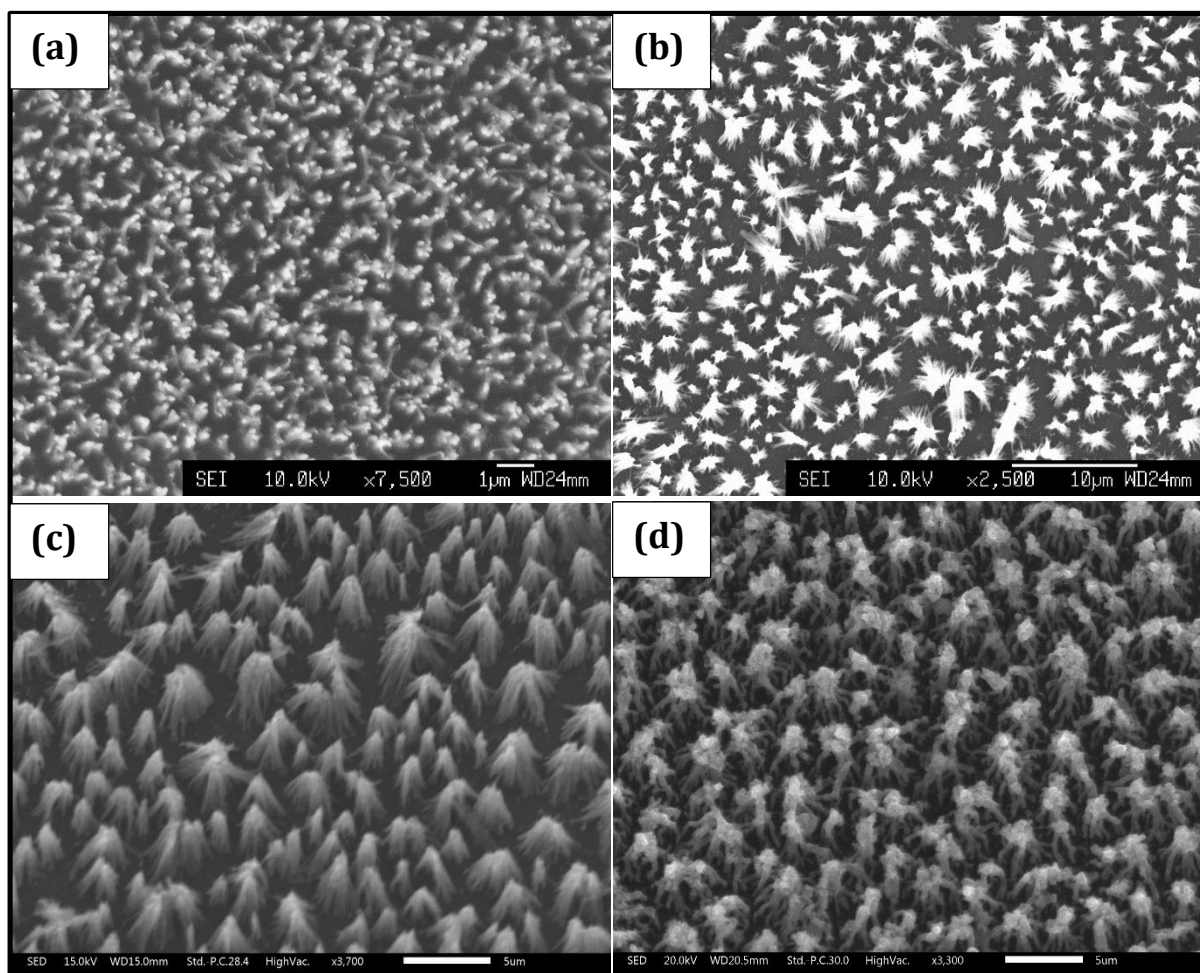


**Figure 3.6** SEM images of (a) VACNTs, (b) top view of electrospayed VACNT teepees, (c) tilted angle view of VACNT teepees, (d) MCD coated teepees.

### 3.1.2 Raman Spectroscopy

Each sample was analysed by Raman spectroscopy exploiting diamond's diagnostic peak at  $1332\text{ cm}^{-1}$  to confirm the deposition of a diamond film and the thickness of the film. Furthermore, Raman spectroscopy also confirmed the presence of boron dopant and the crystallinity of the diamond film due to other characteristic peaks, summarised in table 3.2. An assigned Raman spectra for a NCD film grown on the black silicon needles substrate is shown in Fig. 3.7 with the large silicon peak at  $\sim 500\text{ cm}^{-1}$  removed for clarity. The Raman spectra recorded showed similar peaks throughout.

Raman spectroscopy proved to be particularly useful for analysing the small silicon needles coatings which were often too small to analyse efficiently using SEM. As a result, Raman spectroscopy was primarily used to determine if the small silicon needles had been coated in diamond.

**Table 3.2.** Assignments for peaks commonly observed in Raman spectra of CVD diamond films.<sup>97</sup>

Frequency / ( $\text{cm}^{-1}$ )	Assignment
520	First order silicon Raman peak (silicon is a common substrate for CVD diamond films).
1100 – 1150	Transpolyacetylene at grain boundaries (often visible in NCD CVD diamond films).
1210	Characteristic of a high boron content
1332	Tetrahedral $\text{sp}^3$ diamond band (diagnostic diamond peak).
1345	$\text{sp}^2$ amorphous carbon – D peak (a diagnostic graphite peak)
1430 – 1470	Transpolyacetylene at grain boundaries (often visible in NCD CVD diamond films).
1520 – 1580	$\text{sp}^2$ amorphous carbon – G peak (a diagnostic graphite peak)

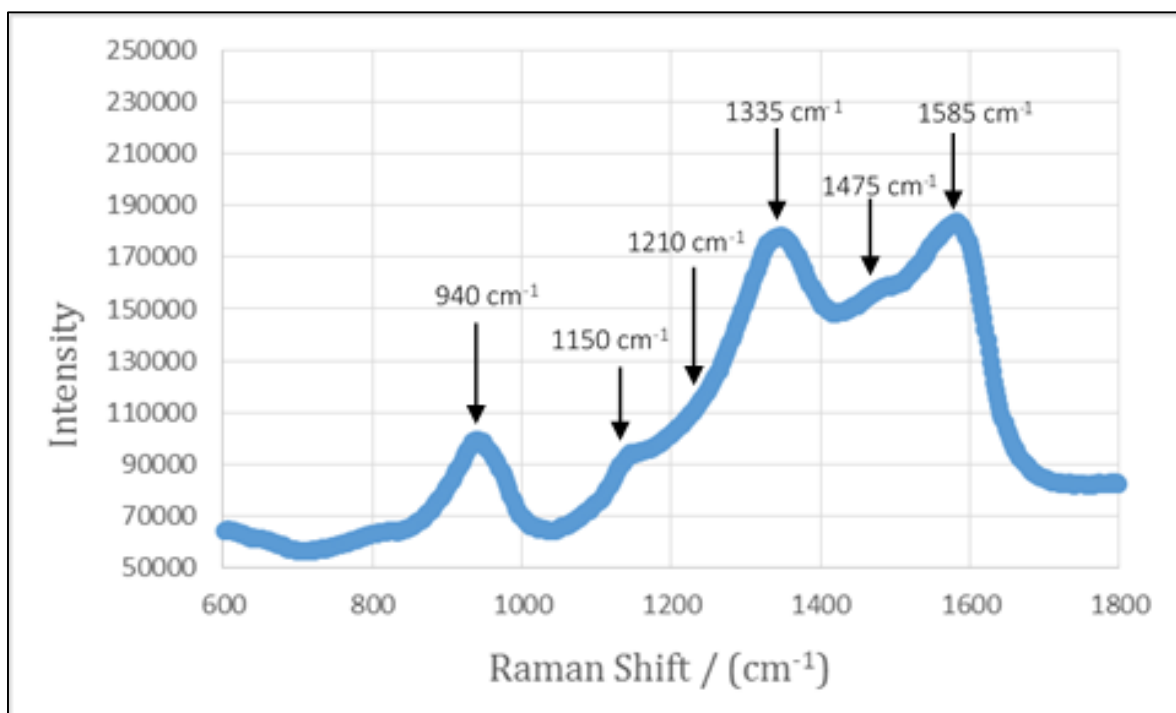


**Figure 3.7.** Green (514 nm) Raman spectrum for a nanocrystalline BDD film, highlighting the second order silicon peak (940  $\text{cm}^{-1}$ ), TPA peaks (1150 & 1475  $\text{cm}^{-1}$ ), high boron content peak (1210  $\text{cm}^{-1}$ ), shifted diamond peak (1335  $\text{cm}^{-1}$ ) and graphite impurity G peak (1585  $\text{cm}^{-1}$ ).

## 3.2 Electrochemistry

A series of experiments were carried out on multiple samples of each nanostructure, as well as a flat BDD electrode for comparison, to analyse the samples electrochemically.

### 3.2.1 Cyclic Voltammetry

The six diamond nanostructures investigated were, flat diamond, small silicon needles, large silicon needles, overgrown silicon needles, VACNT teepees and CNT webs.

### 3.2.1.1 Potassium Nitrate

CVs were first recorded using a simple potassium nitrate solution across a potential window absent of any faradaic current (-0.1 to +0.1 V), recording the capacitive current at a range of scan rates. This was performed for a variety of electrodes of each nanostructure, all showing a larger capacitive current than the flat diamond electrode tested. Fig. 3.8 shows a summary of the CVs recorded for the different nanostructures all appearing quasi-rectangular in shape, characteristic of interfacial double-layer charging, but differing dramatically in magnitude. The largest capacitive current was produced by the overgrown nanostructure, followed by the large needles, CNT webs, CNT teepees, and finally the small needles, whose current differed negligibly from that of the flat diamond electrode.

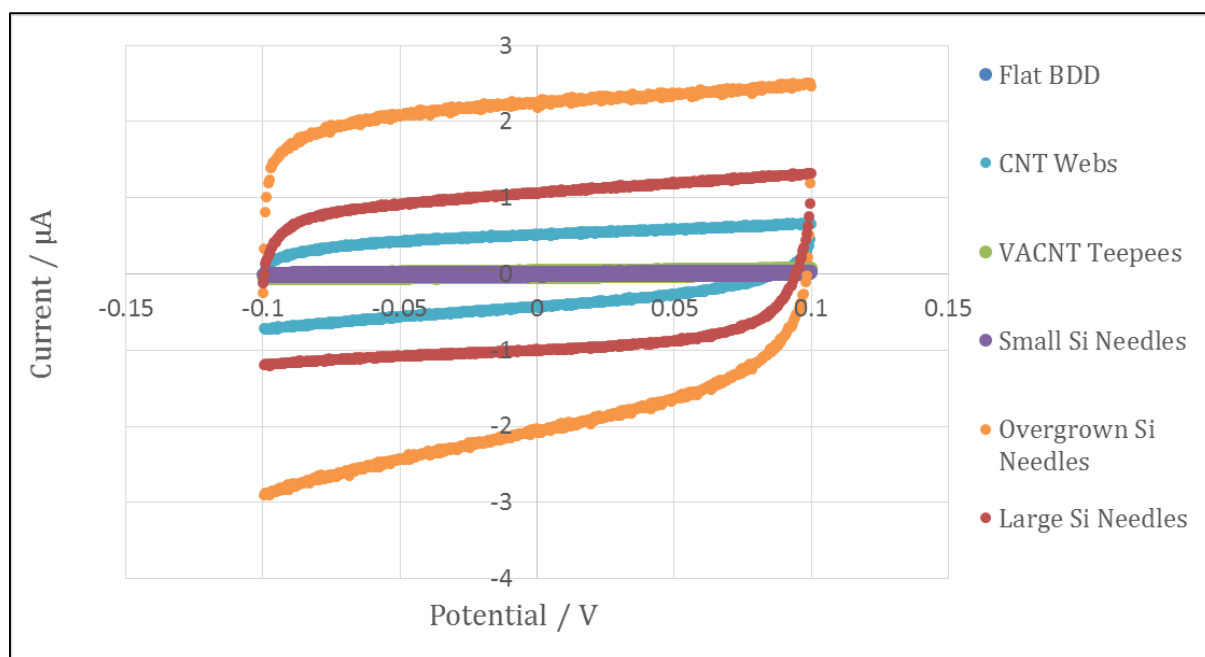


**Figure 3.8.** Cyclic Voltammograms recorded for each nanostructure, at 50 mV/s using 0.1 M potassium nitrate solution.

These data were then used to determine the capacitance of the electrodes, and thus the effective surface area which is directly proportional. The capacitance ( $C$ ) of a capacitor is described in eqn. 3.1, and is related to the voltage ( $V$ ) and charge ( $Q$ ).

$$C = \frac{Q}{V} \quad [3.1]$$

A simple rearrangement, shown in eqn. 3.2, allows for the derivatisation of the current/voltage relationship shown in eqn. 3.3.

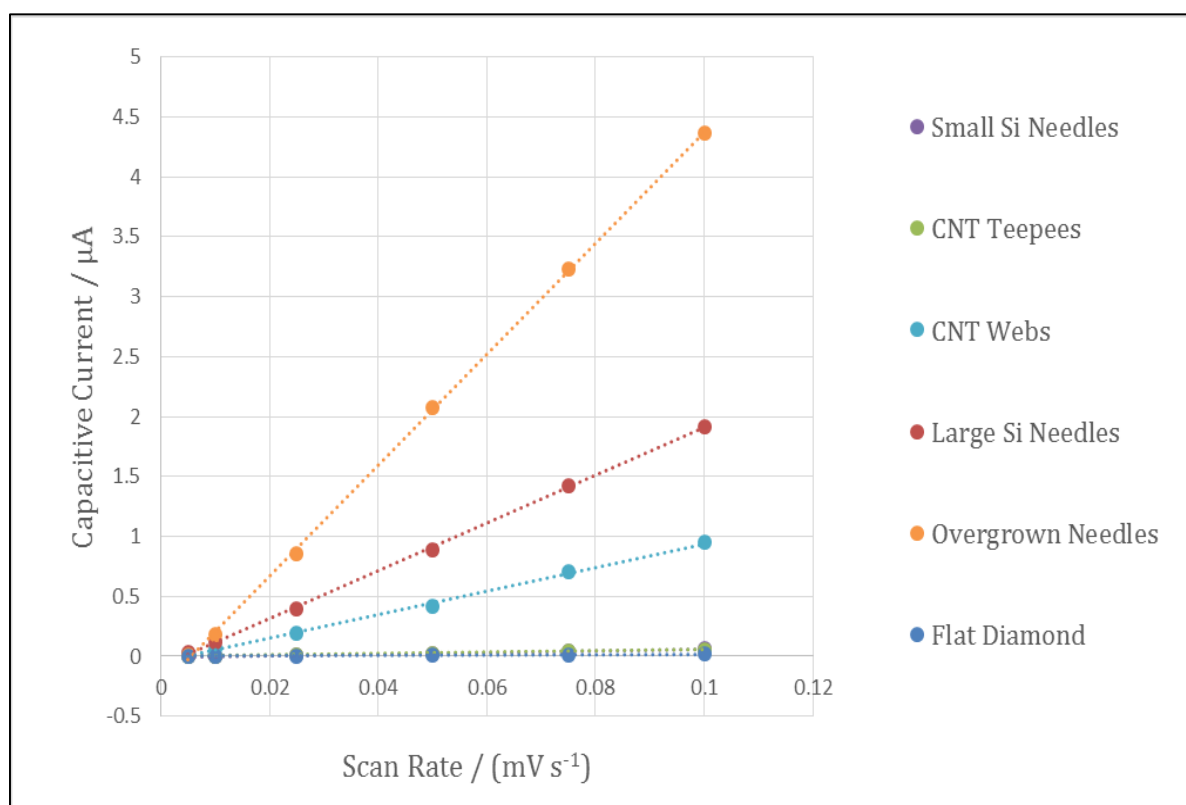
$$Q = CV \quad [3.2]$$

$$I(t) = \frac{dQ}{dt} = C \frac{dV}{dt} \quad [3.3]$$

From this relationship the capacitance for a given geometric area was calculated for each nanostructure, shown in table 3.3, by plotting the peak current ( $dQ/dt$ ) vs scan rate ( $dV/dt$ ) and calculating the gradient, shown in Fig 3.9. Knowing that the effective surface area and the geometric surface area of the flat diamond substrate were approximately equal, it was possible to calculate the effective surface area of each nanostructure, also shown in table 3.3, by using the ratio of the capacitances.

**Table 3.3.** Capacitance and effective surface areas for each nanostructure.

Nanostructure	Capacitance / ( $\mu\text{F cm}^{-2}$ )	Relative Effective Surface Area
Flat Diamond	2.89	1
Small Si Needles	7.56	2.62
CNT Teepees	8.18	2.83
CNT Webs	150.00	51.88
Large Si Needles	279.43	96.64
Overgrown Si Needles	638.00	220.65

**Figure 3.9.** Plots of capacitive current vs scan rate for each nanostructure.

This contradicted the expectation that the shorter the deposition time, the thinner the diamond film, and thus the larger the surface area. One possible explanation for this was that the large silicon needles, although coated in diamond, were not all electrically connected resulting in a lower capacitance.

This was disproved by estimating the effective surface area of the large silicon needles nanostructure, treating each needle as a cone and using simple geometry. The dimensions for an average needle (radius ( $r$ ) =  $0.5 \mu\text{m}$ , height ( $h$ ) =  $5 \mu\text{m}$ ) and the areal density (91 needles  $10 \mu\text{m}^2$ ) were estimated using SEM images, shown below in Fig. 3.10. Using these values and equation 3.4 the estimated effective surface area for the large silicon needles, within the  $7 \text{ mm}^2$  geometric area, was  $546.84 \pm 2 \text{ mm}^2$ . Although this value does not match the experimental value ( $676.48 \text{ mm}^2$ ) exactly, it is similar and is smaller than the value obtained, suggesting that the needles are all electrically connected.

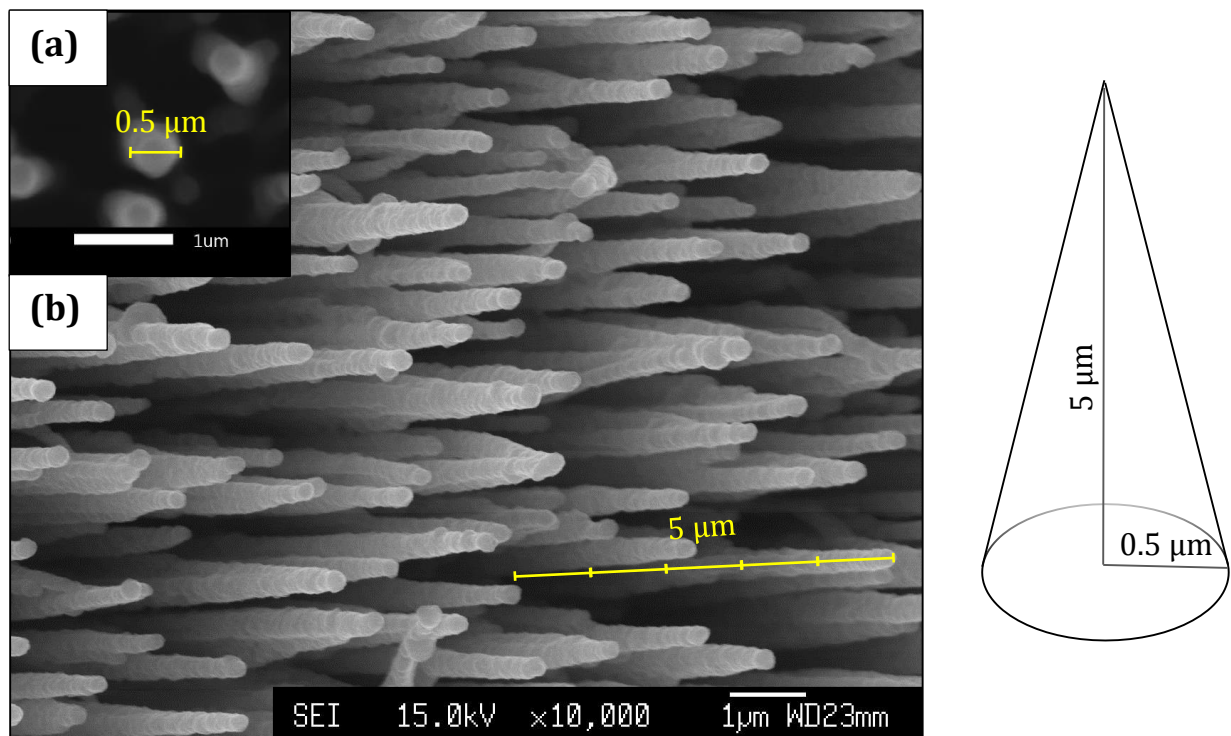


**Figure 3.10.** SEM images used to estimate the dimensions of the large diamond-coated silicon needles including (a) top down view of needles used to estimate radius and (b) tilted view used to estimate height and areal density per  $10 \mu\text{m}^2$ .

$$A = \pi r (r + \sqrt{h^2 + r^2}) \quad [3.4]$$

It is therefore believed that the overgrown needles nanostructure does have a larger surface area, with a possible explanation for this being that the needles had coalesced towards the tip of the needles, with the nanostructure still preserved underneath, effectively adding a porous roof to the nanostructure and thus increasing the surface area.

These results were confirmed separately by Dr H. Zanin at the University of Sao Paolo, who found that the longer deposition times onto the large silicon needles resulted in higher effective surface areas when tested electrochemically using a 0.1 M KCl solution containing 1 mM  $K_3[Fe(CN)_6]$ .

### 3.2.1.2 Potassium Ferricyanide

The most promising sample (highest capacitance) of each nanostructure was then analysed further using a more complex redox system. Excluding the small silicon needles nanostructure, which appeared to show a poor connection (see Fig. 3.11), all six nanostructures were shown to perform electrochemically using a ferri/ferrocyanide redox system, with CNT teepees, CNT webs, large black silicon needles, and the overgrown silicon needles nanostructures producing repeatable CVs over a wide range of scan rates, shown in Fig 3.11. Each of the nanostructures showed slightly different values for the oxidation and reduction peaks, appearing at 0.25 and 0.19 V for the CNT teepees, 0.27 and 0.18 V for the CNT webs, 0.25 and 0.19 V for the large silicon needles, and 0.26 and 0.19 V for the overgrown needles respectively. Again, with the exception of the small silicon needles, all the nanostructures showed a reduced peak-to-peak separation compared to the flat diamond electrode, whose oxidation and reduction peaks were observed at 0.34 and 0.11 V, respectively.

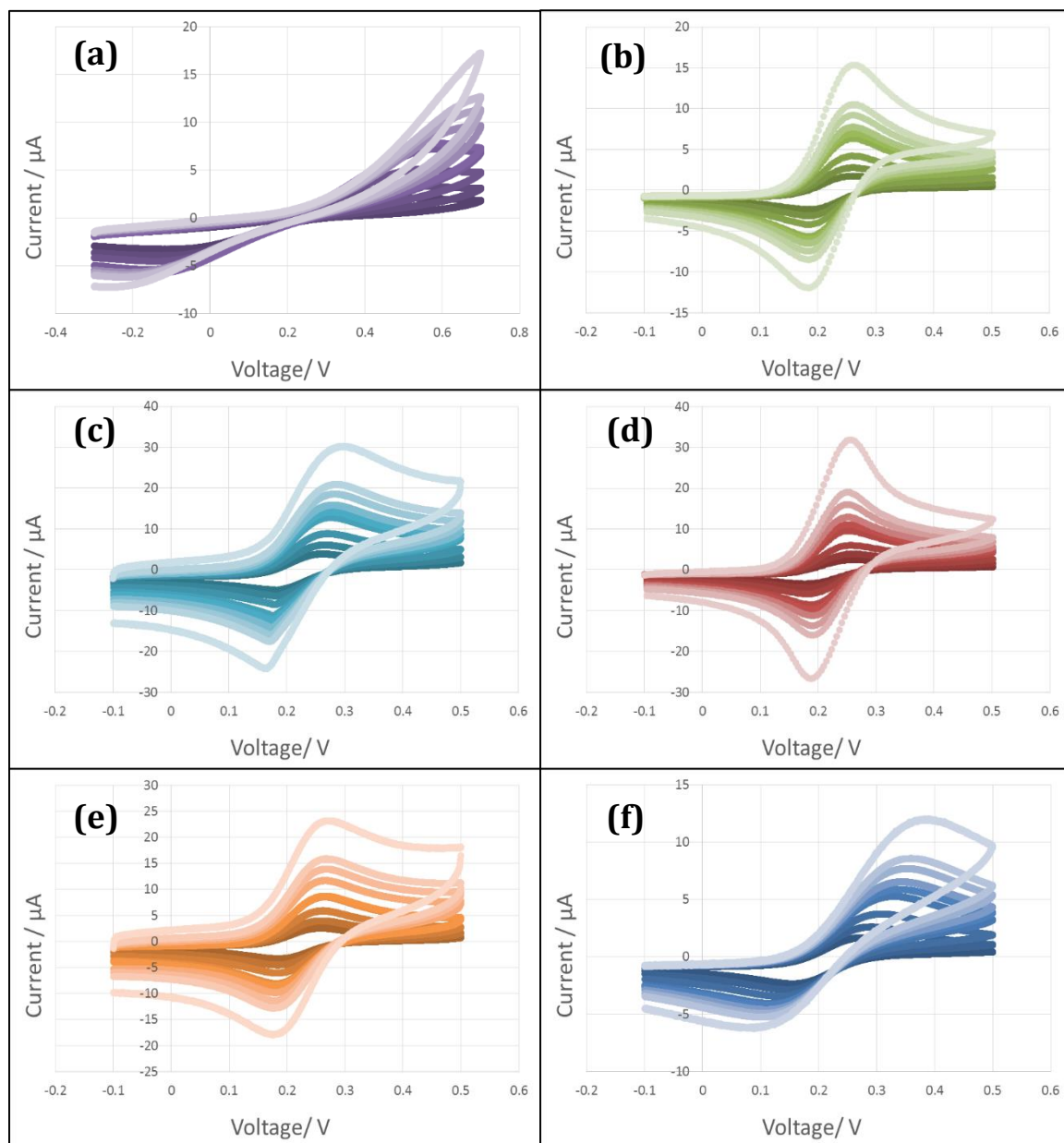


**Figure 3.11.** CVs recorded at different scan rates (dark: 5 mV/s to light: 200 mV/s) using 1 mM  $K_3[Fe(CN)_6]$  in 0.1 M  $KNO_3$  solution using **(a)** small Si needles, **(b)** VACNT teepees, **(c)** CNT webs, **(d)** large Si needles, **(e)** overgrown Si needles and **(f)** flat BDD electrodes.

The nanostructured electrodes anodic and cathodic peaks were independent of scan rate, and when the cathodic peak current was plotted against the square root of the scan rate a linear relationship was shown (Fig. 3.12), both of which are characteristic of a diffusion-controlled reversible process. Two other features characteristic of a one-electron reversible process are a peak-to-peak separation of 59 mV and a cathodic/anodic peak current ratio of 1.

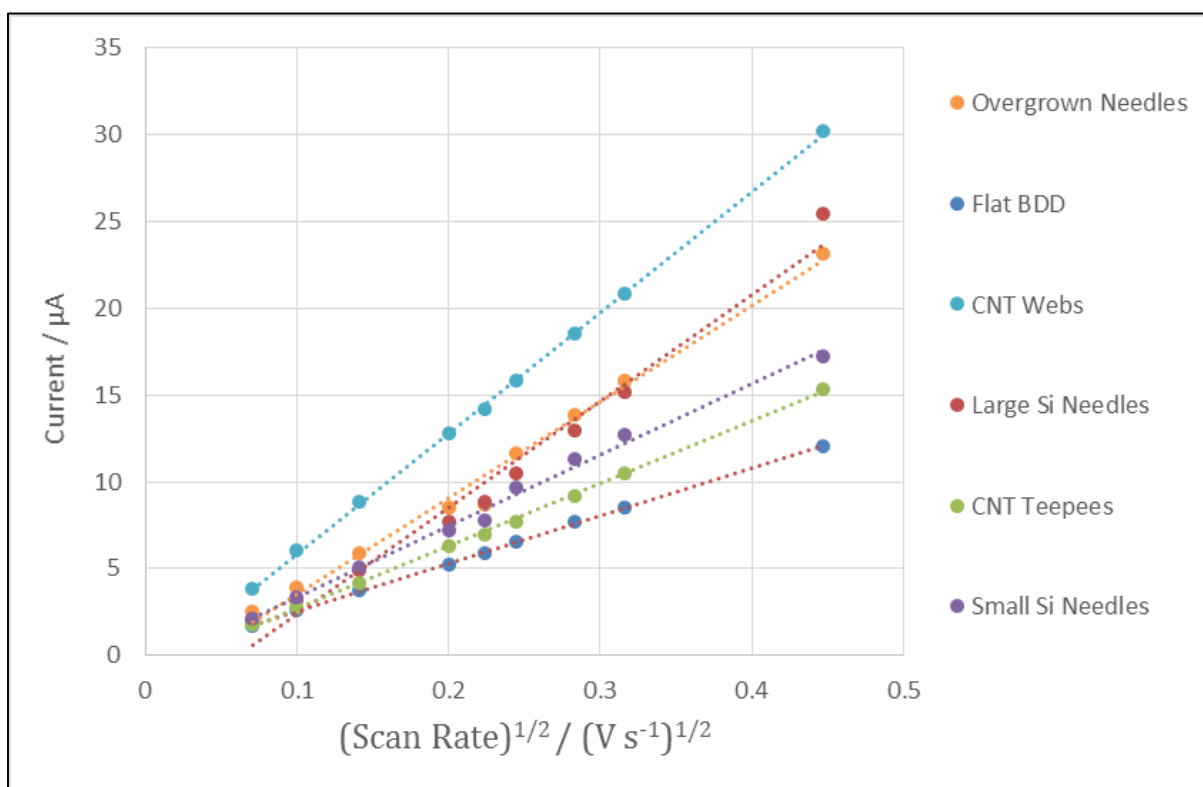


**Figure 3.12.** Plot of peak current vs the square root of the scan rate for each nanostructure, highlighting the linear relationships.

The ratio of cathodic peak current against anodic peak current was calculated for each nanostructure, extrapolating the baselines for each measurement to account for the background solution. Out of the six nanostructures a unity in the peak current ratios was only displayed by the large silicon needles nanostructure with the rest showing slight deviations, in particular the flat and small silicon needles nanostructures. Similar results were found when calculating the peak-to-peak separation, again only the large silicon needles nanostructure displayed a peak-to-peak separation of 59 mV, with all the other nanostructures displaying larger values. This information suggests that a fast electron-transfer mechanism was occurring for the majority of the nanostructures, in particular the large silicon needles, resulting in a diffusion-controlled reversible process. As mentioned previously, this was not the case for the small silicon needles which appeared to have a slow-electron transfer, possibly due to a poor connection.

CVs were then simulated to best fit the data, from which, it was possible to derive values for the diffusion coefficients ( $D$ ) using the normalised current ( $I_{Norm}$ ) values and equation 3.5, where  $n$  is the number of transferred electrons,  $F$  is the faraday constant,  $A$  is the geometric area of the electrode,  $c_{bulk}$  is the bulk concentration,  $V$  is the scan rate,  $R$  is the gas constant, and  $T$  is the temperature. A summary of this sections results are shown in Table 3.4. As can be seen, similar diffusion coefficient values were displayed by the large silicon needles and the flat diamond electrode, further confirming a complete coating.

$$I_{Norm} = nFAc_{bulk} \left( \frac{\pi n F V D}{RT} \right)^{1/2} \quad [3.5]$$

**Table 3.4.** Summary of the results obtained for the ferri/ferrocyanide redox system.

<b>Naonstructure</b>	<b>Oxidation Peak / V</b>	<b>Reduction Peak / V</b>	<b>Peak-to- Peak Separation / V</b>	$I_{p,c} / I_{p,a}$	$I_{Norm}$ / $\mu\text{A}$	$D_R /$ $(\text{cm}^2 \text{s}^{-1})$
Flat Diamond	0.34	0.11	0.23	1.26	5.49	$1.08 \times 10^{-6}$
Small Si Needles	0.58	-0.16	0.74	1.29	5.79	$1.20 \times 10^{-6}$
CNT Teepees	0.25	0.19	0.06	0.94	5.09	$0.93 \times 10^{-6}$
CNT Webs	0.27	0.18	0.09	0.87	1.24	$5.51 \times 10^{-6}$
Large Si Needles	0.25	0.19	0.06	0.96	5.74	$1.18 \times 10^{-6}$
Overgrown Si Needles	0.26	0.19	0.07	0.93	7.65	$2.10 \times 10^{-6}$

Dr H. Zanin at the University of Sao Paulo also carried out electrochemical analysis using the ferri/ferrocyanide redox probe for the black silicon needles electrodes. These results agreed well with those discussed above, with the CVs (shown in Fig 3.13) displaying similar scan rate independent oxidation and reduction peaks, similar peak-to-peak separations, a linear proportionality between peak current and the square root of the scan rate, and also confirmed the electrochemical inactivity of the small silicon needles electrode (due to poor connection and incomplete coating).

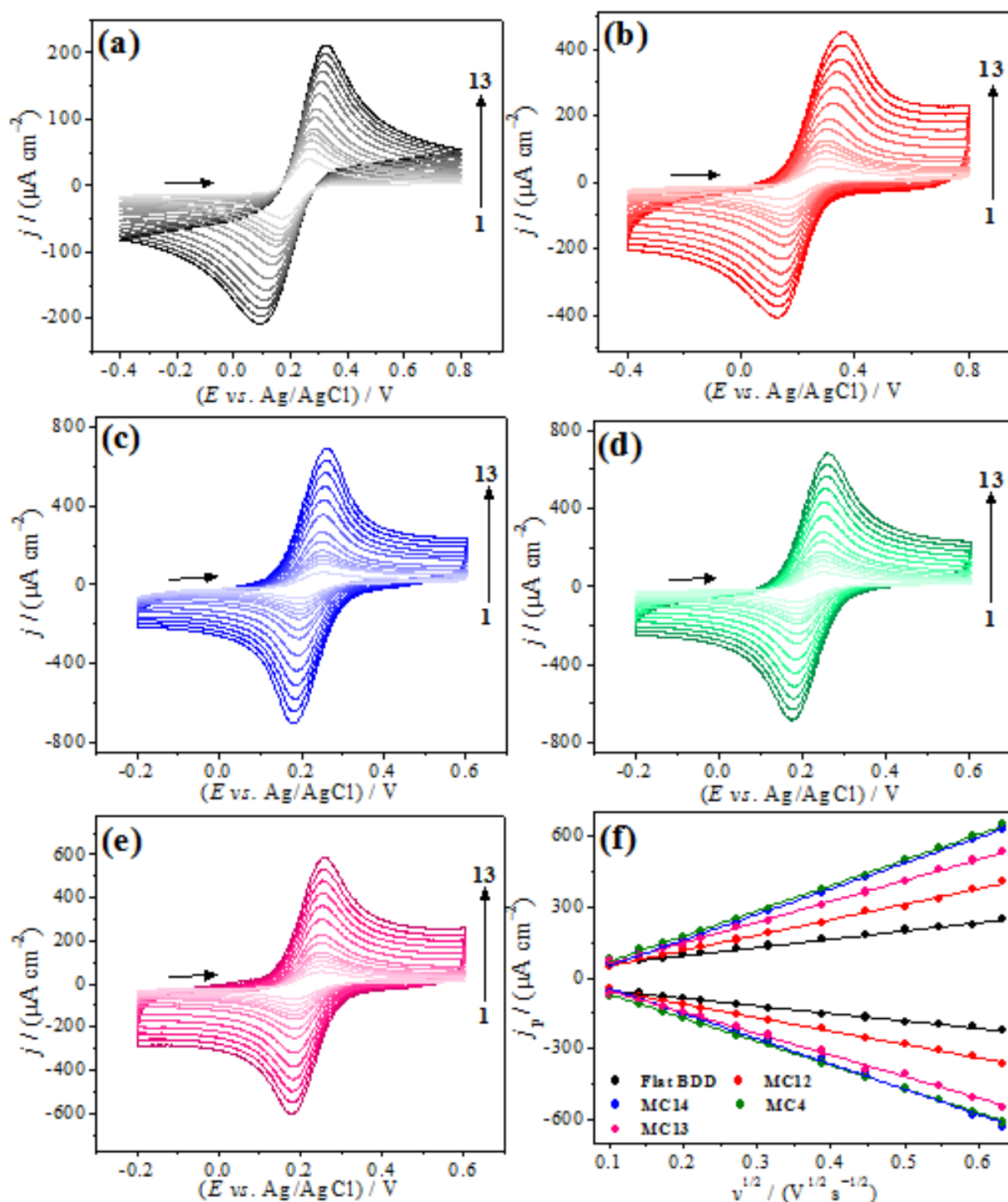


**Figure 3.13.** CVs recorded at different scan rates (1:10 mV/s to 13: 400 mV/s) in 0.1 M KCl solution containing 1 mM  $\text{K}_3[\text{Fe}(\text{CN})_6]$  using **(a)** flat BDD, **(b)** and **(d)** large black silicon needles, **(c)** and **(e)** overgrown silicon needles electrodes. **(f)** Graphics of peak current vs square root of the scan rate obtained for the different BDD electrodes. Courtesy of H. Zanin.

### 3.2.1.3 Dopamine and Uric Acid

Detection of the two biomolecules, dopamine (DA) and uric acid (UA), was then analysed by H. Zanin using the large black silicon needles and overgrown needles electrodes. Both nanostructured electrodes successfully detected the two biomolecules simultaneously and separately, see Fig 3.14, 3.15 and 3.16, over a range of different concentrations, producing linear analytical curves ( $j_p$  vs [DA] and  $j_p$  vs [UA]).

The overgrown silicon needles showed the greatest analytical sensitivity, summarised in table 3.5, with the following detection limits: 0.27  $\mu\text{M}$  for DA and 2.1  $\mu\text{M}$  for UA.

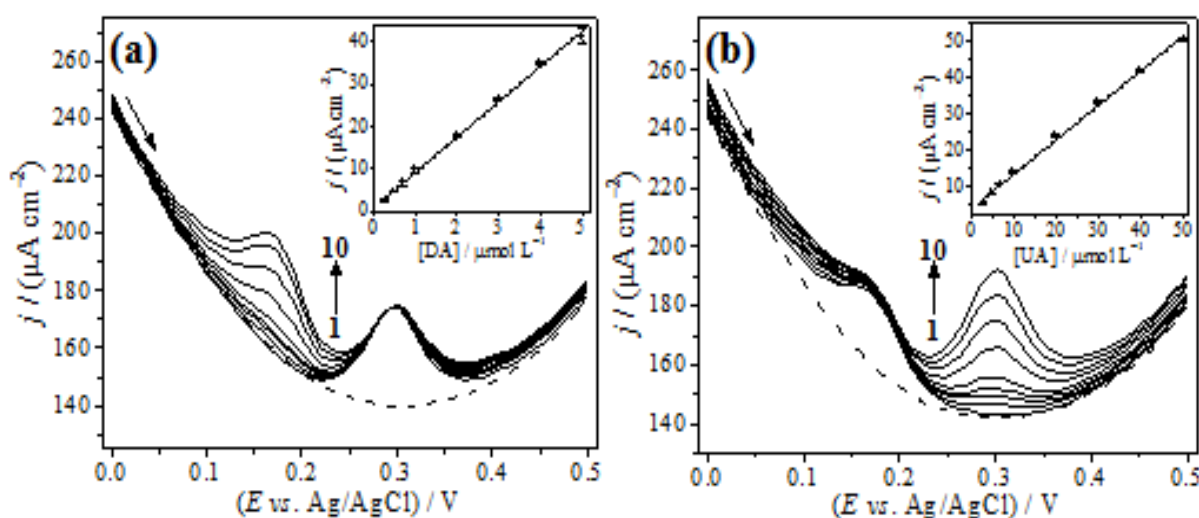


**Figure 3.14.** (a) Differential pulse voltammograms recorded in 0.2 M phosphate buffer solution (pH = 7.0) containing 30  $\mu\text{M}$  UA and different DA concentration levels (1: 0.0 to 10: 5  $\mu\text{M}$ ) using the overgrown silicon needles electrode. Inset: Analytical curve ( $j_p$  vs. [DA]). (b) Differential pulse voltammograms recorded in 0.2 M phosphate buffer solution (pH = 7.0) containing 3  $\mu\text{M}$  DA and different UA concentration levels (1: 0.0 to 10: 50  $\mu\text{M}$ ) using the overgrown silicon needles electrode. Inset: Analytical curve ( $j_p$  vs. [UA]). Courtesy of H. Zanin.

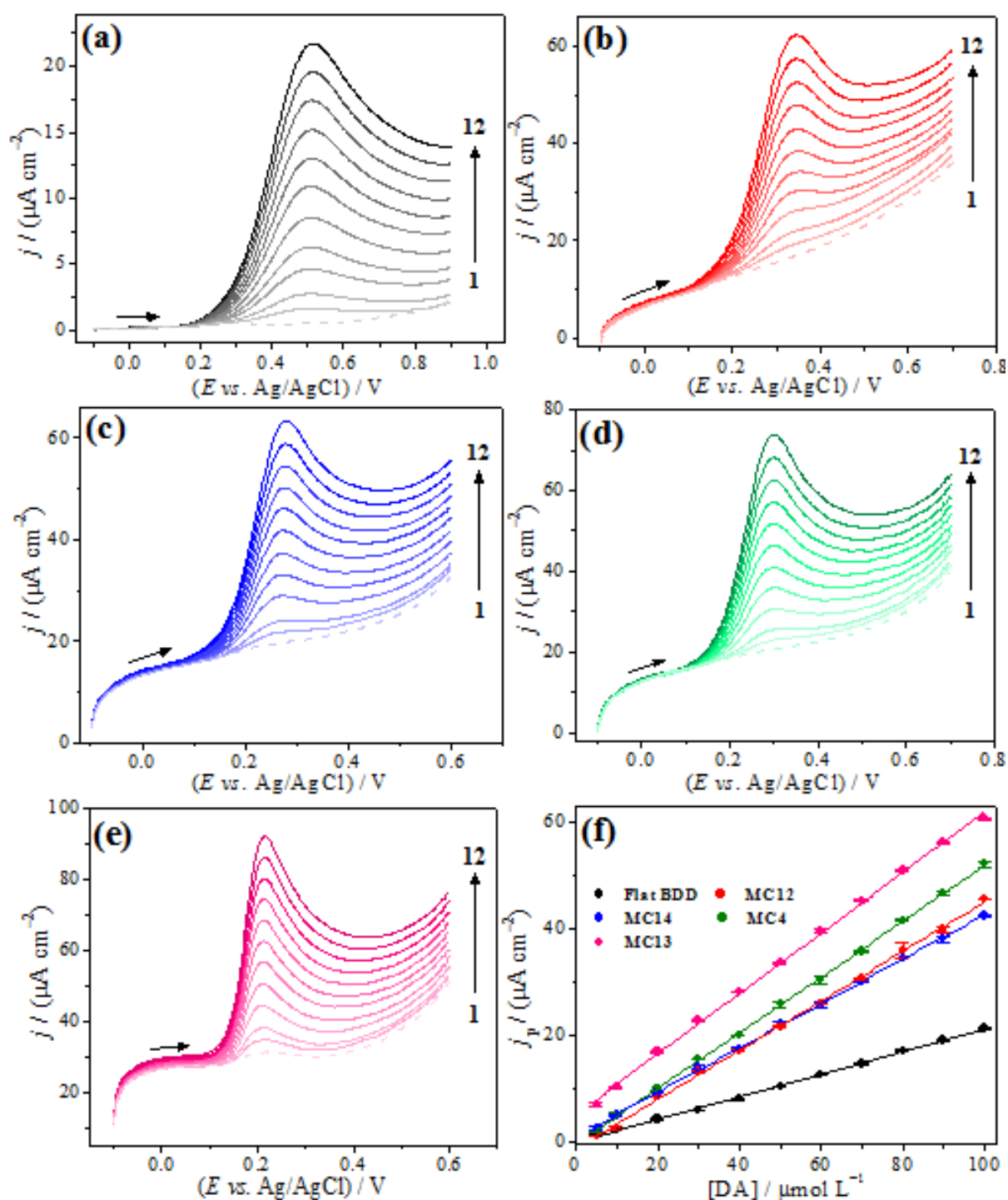


**Figure 3.15.** Linear sweep voltammograms recorded in 0.2 M phosphate buffer solution (pH = 7.0) containing different DA concentration levels (1: 0.0 to 12: 0.1 mM) using (a) flat BDD, (b) and (d) large black silicon needles, (c) and (e) overgrown silicon needles electrodes. (f) Analytical curves obtained for DA using different BDD electrodes. Courtesy of H. Zanin.

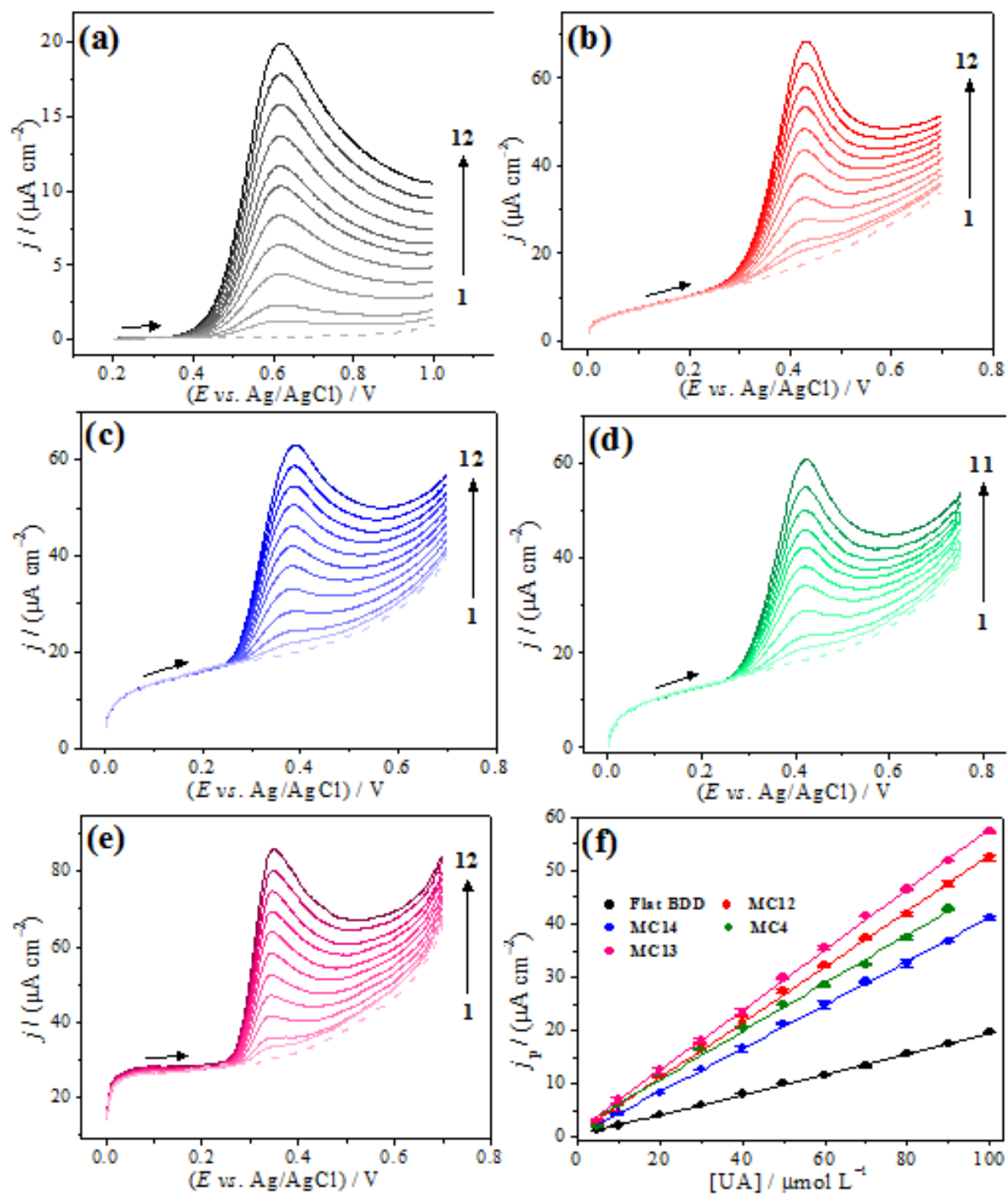


**Figure 3.16.** Linear sweep voltammograms recorded in 0.2 M phosphate buffer solution (pH = 7.0) containing different UA concentration levels (1: 0.0 to 12: 0.1 mM) using **(a)** flat BDD, **(b)** and **(d)** large black silicon needles, **(c)** and **(e)** overgrown silicon needles electrodes. **(f)** Analytical curves obtained for UA using different BDD electrodes. Courtesy of H. Zanin.

**Table 3.5** Analytical Sensitivity towards DA and UA. Values displayed are from the highest sample of each nanostructure. Courtesy of H. Zanin.

Electrode	Analytical sensitivity ( $\mu\text{A cm}^{-2} \text{mol}^{-1} \text{L}$ )	
	DA	UA
Flat BDD	$2.12 \times 10^5$	$1.91 \times 10^5$
Large Silicon Needles	$5.22 \times 10^5$	$4.54 \times 10^5$
Overgrown Silicon Needles	$5.67 \times 10^5$	$5.67 \times 10^5$

### 3.2.2 Electrochemical Impedance Spectroscopy

EIS was performed on a sample of each of the nanostructured electrodes using a frequency response analyser to measure the impedance ( $Z$ ) of each electrode at various frequencies. These measurements were performed at the formal potential of the redox system (0.221 V) determined during cyclic voltammetry measurements. A Nyquist plot of the data is shown in Fig 3.17, with the imaginary component ( $Z''$ ) of impedance plotted on the vertical axis, and the real component ( $Z'$ ) plotted on the horizontal axis. Bode plots are also included, shown in Fig 3.17, where the impedance and phase angle are plotted against the frequency. The small silicon needles nanostructure has been excluded from these plots due to it causing an obscuration in the other curves.

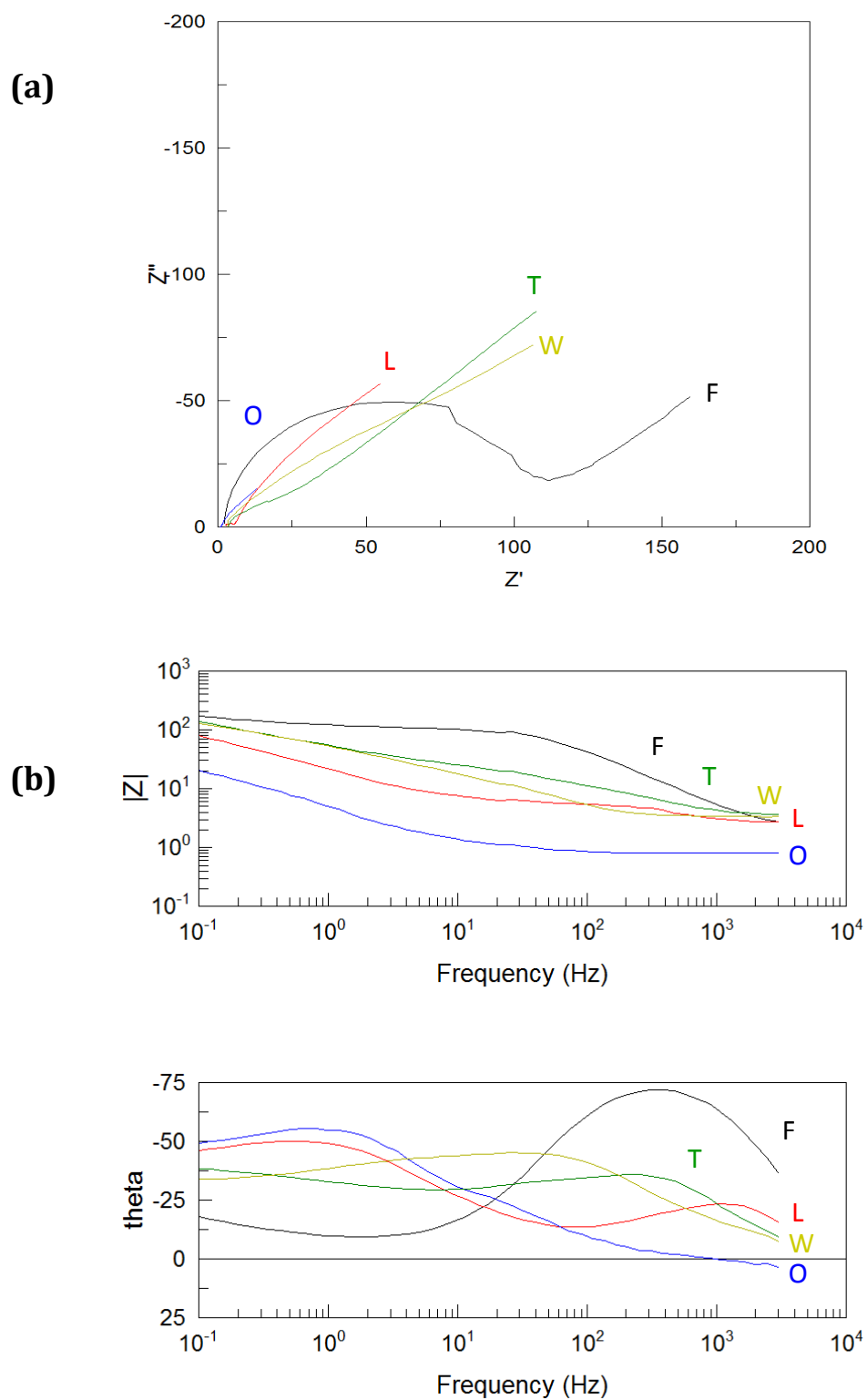


**Figure 3.17.** (a) Nyquist plot and (b) Bode plots of the impedance measurements recorded for the flat diamond (F), overgrown silicon needles (O), large silicon needles (L), CNT teepees (T), and CNT Webs (W) nanostructures.

Impedance, similarly to resistance, describes a circuit's ability to resist the flow of charge. Unlike resistance, however, impedance also accounts for the reactance of a system, most notably the inductance and capacitance, and can therefore be used with more complex systems where resistance fails.

The impedance of a system is inversely proportional to the capacitance and therefore can be used as another method for determining the capacitance of the different nanostructured electrodes. As shown in Fig. 3.17 (b) the lowest impedance, and thus the highest capacitance, was displayed by the overgrown silicon needles followed by, large silicon needles, CNT webs, CNT teepees and finally the flat diamond electrode. This provided a qualitative analysis of the nanostructures capacitances, and agreed well with the values calculated using cyclic voltammetry earlier.

Through the use of resistors and capacitors it is possible to model the physical and chemical properties of an electrochemical system. Therefore, EIS data can be fitted to an equivalent electrical circuit model to obtain quantitative values for the capacitance of the system. This analysis has not been performed, but a suggested equivalent electrical circuit (Randles Circuit) is shown in Fig 3.18, consisting of two resistors  $R_s$  and  $R_{ct}$ , a capacitor  $C_{dl}$  and a Warburg impedance  $Z_w$ , which represent the electrolyte solutions resistance, charge transfer resistance, double-layer capacitance of the electrode, and the diffusion of the electrolyte, respectively.

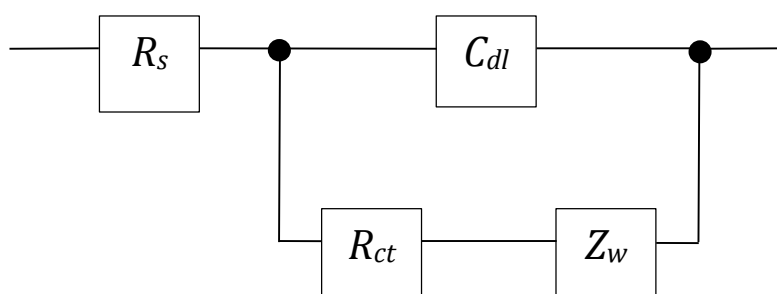
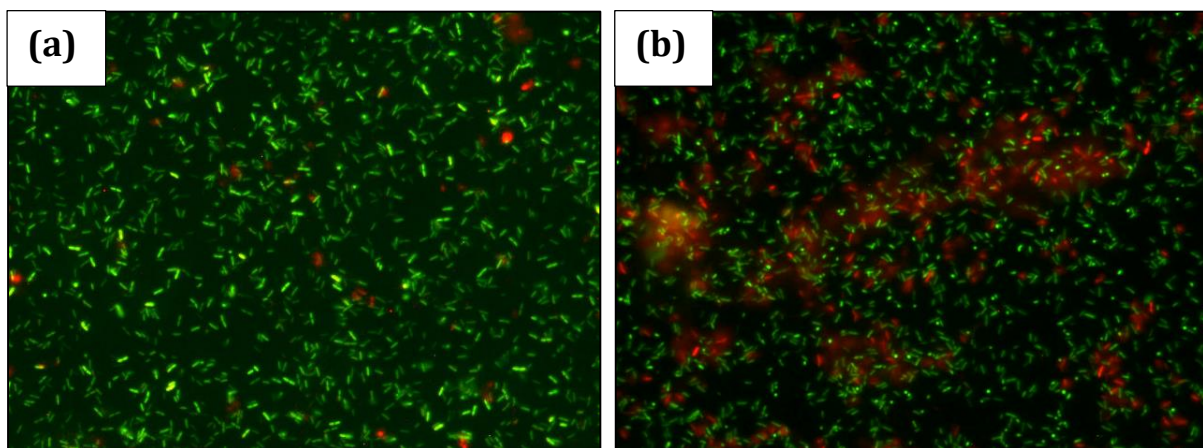


**Figure 3.18.** Schematic diagram of a suggested electrical circuit that could potentially be used to model the impedance data recorded.

### 3.3 Bactericidal Activity

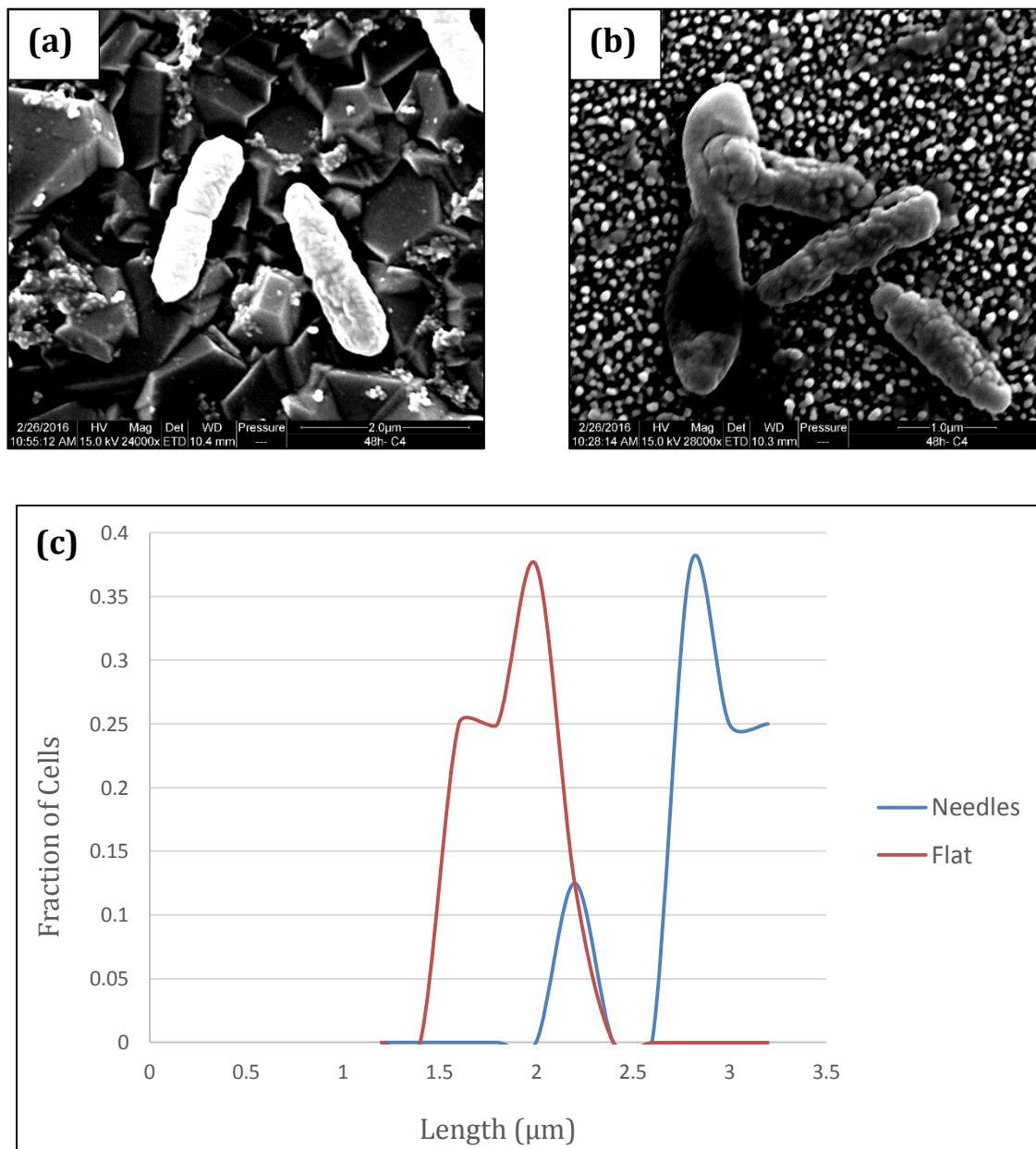
The diamond coated small silicon needles were tested by Dr G. Hazell in the School of Oral and Dental Sciences using the procedure outlined in section 2.3. Using Live/Dead viability stain it was possible to simultaneously stain viable cells with calcein-AM (green fluorescence) and dead cells with propidium iodide (red fluorescence) solutions. Viable cells uptake the lipophilic calcein-AM and metabolise it into the fluorescent calcein, resulting in green fluorescence by only viable cells. Propidium iodide, on the other hand, struggles to transverse a viable cell membrane and instead can only pass through the more disordered regions of a dead cell membrane, resulting in red fluorescence only in dead cells.

Fig. 3.19 shows the diamond-coated small needles sample in comparison to a flat silicon sample, viewed under an optical microscope. As can be seen, the diamond-coated needles showed an increase in cell deaths compared to a flat silicon sample, confirming the surface's bactericidal properties. Several repeats were carried out and the overall increase of dead cells at the surface was quantified as approximately 10% after 1 hour of incubation, which is comparable to other nanostructured antibacterial surfaces.<sup>98</sup>



**Figure 3.19.** Optical microscope images of alive (green) and dead (red) bacteria on **(a)** flat silicon sample and **(b)** diamond coated small silicon needles sample. Courtesy of G. Hazell.

An increase in dead cells was further confirmed by an increased cell length distribution, of approximately 2  $\mu\text{m}$  (healthy cell) to 2.8  $\mu\text{m}$ , corresponding to the rupturing and death of the cell, shown via SEM images and quantified in Fig. 3.20.



**Figure 3.20.** SEM images of (a) viable bacteria cells on the flat silicon surface and (b) dead cells on the diamond coated needles surface highlighting a rupturing of the cell membrane and loss of turgidity. (c) Cell length distribution for bacteria on the flat silicon sample and the diamond coated small silicon needles sample. Courtesy of G. Hazell.

## 4. Conclusions and Future Work

---

### 4.1 Conclusions

The primary aim of the project was to fabricate a range of high surface area BDD electrodes, varying in thickness and crystallinity, and to characterise them by SEM, laser Raman, and electrochemically.

This was achieved producing 30+ electrodes in total across the four nanostructures, with each nanostructure being successfully coated in micro and nanocrystalline diamond. Two of each electrode were produced allowing for the samples to be analysed by myself and also electrochemically by Dr H. Zanin (working at the University of Sao Paulo in Brazil). The crystallinity and composition of each film was analysed by SEM and confirmed using laser Raman.

As well as being analysed electrochemically by H. Zanin a multiple of electrodes of each nanostructure were analysed electrochemically by myself using cyclic voltammetry to calculate diffusion coefficients, double-layer capacitances and effective surface areas. Impedance measurements were then also used to confirm the capacitance values measured, indicating that the overgrown silicon needles nanostructure had the highest capacitance and effective surface area followed by the large silicon needles, CNT webs, CNT teepees, and finally the small silicon needles.

The overgrown silicon needles nanostructure possessed a capacitance and effective surface area of over 220 times greater than that of a flat BDD electrode, and would therefore be the most suitable for electrochemical applications such as detecting water contaminants and drug detection. This was confirmed by H. Zanin and demonstrated by detecting two biomolecules, dopamine and uric acid, at concentrations as low as 0.27  $\mu\text{M}$  and 2.1  $\mu\text{M}$  respectively.

A range of antibacterial surfaces were also fabricated using two methods, deposition of diamond onto the small silicon needles, and prolonged growth of diamond onto large silicon needles. Primary tests performed by Dr G. Hazell (of the School of Oral and Dental

Sciences) into the bactericidal properties of these surfaces shows promise, increasing the concentration of dead cells by 10% after 1 hour of incubation.

## 4.2 Future Work

A range of further work could be carried out to further optimise the silicon needles nanostructures. Some suggestions include:

- Attempt to develop longer silicon needles by prolonging the etching time and again attempt to diamond coat. This would enhance the surface area of the electrodes further whilst also allowing for thicker diamond films to be deposited before the needles are overgrown, increasing the durability of the electrodes and their ability to form a connection.
- Attempt to grow silicon needles using conductive silicon and investigate how they perform electrochemically.
- Attempt to form a better connection with the small silicon needles nanostructure, perhaps using a seeding pretreatment and shorter deposition time in order to achieve a more complete coating.

Further analysis of the samples could also be carried out including:

- Modelling the impedance data, most likely using a Randles circuit, to quantitatively confirm the capacitance values recorded.
- Investigating the field emission properties of each of the nanostructures. Diamond's minute/negative electron affinity combined with the large surface area of the electrodes could be used in field emission devices.

Upon finishing the project only one sample had been tested for bactericidal properties, and although the results showed promise there is still a large scope for investigation.

Some suggestions include:

- Testing more antibacterial surface samples. Testing of more samples would provide a greater idea of the efficacy of the surfaces, how they can be optimised for applications, and further insight into the mechanism of cell death. This includes testing samples of varied needle height, grown by either depositing diamond

directly onto silicon needles of various heights, or controlling the needle height by prolonging the growth of diamond onto the larger needles.

- Investigating the durability of the surfaces, in particular their resistance to touch. This could provide information on whether the nanostructures are easily damaged, how their bactericidal properties vary with damage, and the viability of any potential applications.

## 5. References

---

- <sup>1</sup> D. Shriver, M. Weller, T. Overton, J. Rourke and F. Armstrong, *Inorganic Chemistry*, Oxford University Press, Great Britain, 6th edn., 2014
- <sup>2</sup> N. N. Greenwood and A. Earnshaw, *Chemistry of the Elements*, Butterworth-Heinemann, Oxford, 2nd edn., 1997
- <sup>3</sup> O.A. Williams, *Diamond Relat. Mater.*, 2011, **20**, 621
- <sup>4</sup> X. Liu, G. Zhang and Y. Zhang, *Carbon*, 2015, **94**, 760
- <sup>5</sup> E. Woerner, C. Wild, W. Mueller-Sebert and P. Koidl, *Diamond Relat. Mater.*, 2001, **10**, 557
- <sup>6</sup> Y. Zou, P. W. May, S. M. C. Vieira and N. A. Fox, *J. Appl. Phys.*, 2012, **112**, 044903
- <sup>7</sup> H. Liu and D. S. Dandy, *Diamond Chemical Vapor Deposition Nucleation and Early Growth Stages*, Noyes Publications, New Jersey, 1995
- <sup>8</sup> E. Brillas and C. Huitle, *Synthetic Diamond Films Preparation, Electrochemistry, Characterization, and Applications*, John Wiley & Sons. Hoboken, 2011
- <sup>9</sup> F. A. Almeida, J. M. Carrapichano, A. J. S. Fernandes, J. Sacramento, R. F. Silva and F. J. Oliveira, *Int. J. Refract. Met. Hard Mater.*, 2011, **29**, 618
- <sup>10</sup> M. Tadjer, T. Anderson, K. Hobart, T. Feygelson, J. Caldwell, C. Eddy, F. Kub, J. Butler, B. Pate and J. Melngailis, *IEEE Electron Device Lett.*, 2012, **33**, 23
- <sup>11</sup> T. Sharda, M. M. Rahaman, Y. Nukaya, T. Soga, T. Jimbo and M. Umeno, *Diamond Relat. Mater.*, 2001, **10**, 561
- <sup>12</sup> S. Jeedigunta, Ph.D. Thesis, University of South Florida, 2008
- <sup>13</sup> Q. Liang, A. Stanishevsky and Y. K. Vohra, *Thin Solid Films*, 2008, **517**, 800
- <sup>14</sup> T. Zhang, X. Liu, F. Sun and Z. Zhang, *J. Cryst. Growth*, 2015, **426**, 15
- <sup>15</sup> D. Reinhard, T. Grotjohn, M. Becker, M. Yaran, T. Schuelke and J. Asmussen, *J. Vac. Sci. Technol. B: Microelectron. Nanometer Struct. –Process., Meas., Phenom.*, 2004, **22**, 2811

- 
- <sup>16</sup> A. J. S. Fernandes, M. A. Neto, F. A. Almeida, R. F. Silva and F. M. Costa, *Diamond Relat. Mater.*, 2007, **16**, 757
- <sup>17</sup> P. W. May and Y. A. Mankelevich, *J. Appl. Phys.*, 2006, **100**, 24301
- <sup>18</sup> T. Hao, H. Zhang, C. Shi and G. Han, *Surf. Coat. Technol.*, 2006, **201**, 801
- <sup>19</sup> Y. Liu, Y. Tzeng, C. Liu, P. Tso and I. Lin, *Diamond Relat. Mater.*, 2004, **13**, 1859
- <sup>20</sup> J. C. Angus, H. A. Will and W. S. Stanko, *J. Appl. Phys.*, 1968, **39**, 2915
- <sup>21</sup> G. F. Zhang, X. Zheng and Z. T. Liu, *J. Cryst. Growth.*, 1993, **133**, 117
- <sup>22</sup> W. A. Yarbrough and R. Messier, *Science*, 1990, **247**, 688
- <sup>23</sup> S. G. Ansari, M. A. Dar, Y. Kim, H. Seo, G. Kim, R. Wahab, Z. A. Ansari, J. Seo and H. Shin, *Korean. J. Chem. Eng.*, 2008, **25**, 593
- <sup>24</sup> C. M. niu, G. Tsagaropoulos, J. Baglio, K. Dwight and A. Wold, *J. Solid State Chem.*, 1991, **91**, 47
- <sup>25</sup> G. Benedek, P. Milani and V. G. Ralchenko, *Nanostructured Carbon for Advanced Applications*, Kluwer Academic Publishers, Netherlands, 2001
- <sup>26</sup> V. Ralchenko, A. Seveliev, S. Voronina, a. Dementjev, K. Maslakov, M. Salerno, A. Podesta and P. Milani, in *Synthesis, Properties and Applications of Ultrananocrystalline Diamond*, ed. D. M. Gruen, O. A. Shenderova and A. Y. Vul, Springer, Dordrecht, 2004, vol. 192, ch. 9, pp. 109-124
- <sup>27</sup> O. J. L. Fox, J. O. P. Holloway, G. M. Fuge, P. W. May and M. N. R. Ashfold, *Mater. Res. Soc. Symp. Proc.*, 2010, **1203**, 53
- <sup>28</sup> P. W. May, *Phil. Trans. R. Soc. Lond. A*, 2000, **358**, 473
- <sup>29</sup> P. W. May, W. J. Ludlow, M. Hannaway, P. J. Heard, J. A. Smith and K. N. Rosser, *Diamond Relat. Mater.*, 2008, **17**, 105
- <sup>30</sup> K. Okano, H. Naruki, Y. Akiba, T. Kurosu, M. Iida and Y. Hirose, *Jpn. J. Appl. Phys.*, 1988, **27**, 15
- <sup>31</sup> S. A. Grot, G. S. Gildenblat, C. W. Hatfield, C. R. Wronski, A. R. Badzian, T. Badzian and R. Messier, *IEEE Electron Device Lett.*, 1990, **11**, 100
- <sup>32</sup> A. T. Collins, in *Properties and Growth of Diamond*, ed. G. Davies, INSPEC, London, 1994, ch. 9, pp. 261-288

- 
- <sup>33</sup> A. Kraft, *Int. J. Electrochem. Sci.*, 2007, **2**, 355
- <sup>34</sup> K. Okano, S. Koizumi, S. R. P. Silva and G. A. J. Amaratunga, *Nature*, 1996, **381**, 140
- <sup>35</sup> A. T. Sowers, B. L. Ward, S. L. English and R. J. Nemanich, *J. Appl. Phys.*, 1999, **86**, 3973
- <sup>36</sup> S. Koizumi, T. Teraji and H. Kanda, *Diamond Relat. Mater.*, 2000, **9**, 935
- <sup>37</sup> Y. Mukuda, T. Watanabe, A. Ueda, Y. Nishibayashi and Y. Einaga, *Electrochim. Acta.*, 2015, **179**, 599
- <sup>38</sup> M. Nesladek, *Semicond. Sci. Technol.*, 2005, **20**, R19
- <sup>39</sup> A. Gicquel, K. Hassouni, F. Silva and J. Achard, *Curr. Appl. Phys.*, 2001, **1**, 479
- <sup>40</sup> C. Nebel and J. Ristein, *Thin-Film Diamond II Semiconductors and Semimetals*, Elsevier Academic Press, Amsterdam, 2004
- <sup>41</sup> R. Kiran, E. Scorsone, J. Sanoit, J. C. Arnault, P. Mailley and P. Bergonzo, *J. Electrochem. Soc.*, 2013, **160**, H67
- <sup>42</sup> S. Park, G. Kim, J. Parl, Y. Einaga and A. Fujishima, *J. New Mater. Electrochem. Syst.*, 2005, **8**, 65
- <sup>43</sup> N. Spataru, B. V. Sarada, D. A. Tryk and A. Fujishima, *Electroanalysis*, 2002, **14**, 721
- <sup>44</sup> C. E. Troupe, I. C. Drummond, C. Graham, J. Grice, P. John, J. I. B. Wilson, M. G. Jubber and N. A. Morrison, *Diamond Relat. Mater.*, 1998, **7**, 575
- <sup>45</sup> O. Chailapakul, E. Popa, H. Tai, B. V. Sarada, D. A. Tryk and A. Fujishima, *Electrochem. Commun.*, 2000, **2**, 422
- <sup>46</sup> B. V. Saranda, T. N. Rao, D. A. Tryk and A. Fujishima, *Anal. Chem.*, 2000, **72**, 1632
- <sup>47</sup> E. Popa, D. A. Tryk and A. Fujishima, *Diamond Materials VI*, 2000, **99**, 512
- <sup>48</sup> R. Channon, M. Joseph, E. Bitziou, A. Bristow, A. Ray and J. Macpherson, *Anal. Chem.*, 2015, **87**, 10064
- <sup>49</sup> G. Mansano, A. Eisele, L. Dall'Antonia, S. Afonso and E. Sartori, *J. Electroanal. Chem.*, 2015, **738**, 188
- <sup>50</sup> M. Alfaro, S. Ferro, C. Huitle and Y. Vong, *J. Braz. Chem. Soc.*, 2006, **17**, 227
- <sup>51</sup> J. Utrilla, M. Polo, M. García, G. Joya and R. Pérez, *Chemosphere*, 2013, **93**, 1268
- <sup>52</sup> M. Gattrell, D. W. Kirk, *Can. J. chem. Eng.*, 1990, **68**, 997

- 
- <sup>53</sup> B. Correa-Lozano, C. Comninellis and A. De Battisti, *J. Appl. Electrochem.*, 1997, **27**, 970
- <sup>54</sup> O. Simond and C. Comninellis, *Electrochim. Acta.*, 1997, **42**, 2013
- <sup>55</sup> C. Huitle, *Mat. Res.*, 2007, **10**, 419
- <sup>56</sup> M. Gumpu, S. Sethuraman, U. Krishnan and J. Rayappan, *Sens. Actuators*, 2015, **213**, 515
- <sup>57</sup> P. Chooto, P. Wararatananurak and C. Innuphat, *ScienceAsia*, 2010, **36**, 150
- <sup>58</sup> T. Arantes, A. Sardinha, M. Baldan, F. Cristovan and N. Ferreira, *Talanta*, 2014, **128**, 132
- <sup>59</sup> R. S. Sussmann, *CVD Diamond, for Electronic Devices and Sensors*, John Wiley and Sons, United Kingdom, 2009
- <sup>60</sup> J. Iniesta, P. A. Michaud, M. Panizza, G. Cerisola, A. Aldaz and C. Comninellis, *Electrochim. Acta.*, 2001, **46**, 3573
- <sup>61</sup> E. A. McGaw and G. M. Swain, *Anal. Chim. Acta.*, 2006, **575**, 180
- <sup>62</sup> P. Sonthalia, E. McGaw, Y. Show and G. M. Swain, *Anal. Chim. Acta.*, 2004, **522**, 35
- <sup>63</sup> D. Dragoe, N. Spătaru, R. Kawasaki, A. Manivannan, T. Spătaru, D. A. Tryk and A. Fujishima, *Electrochim. Acta.*, 2006, **51**, 2437
- <sup>64</sup> J. Iniesta, P. A. Michaud, M. Panizza, G. Cerisola, A. Aldaz and C. Comninellis, *Electrochim. Acta.*, 2001, **46**, 3573
- <sup>65</sup> J. Iniesta, P. A. Michaud, M. Panizza and C. Comninellis, *Electrochem. Commun.*, 2001, **3**, 346
- <sup>66</sup> P. A. Michaud, E. Mahe, W. Haenni, A. Perret and C. Comninellis, *Electrochem. Solid-State Lett.*, 2000, **3**, 77
- <sup>67</sup> M. S. Saha, T. Furuta and Y. Nishiki, *Electrochem. Solid-State Lett.*, 2003, **6**, D5
- <sup>68</sup> M. Panizza and G. Cerisola, *Electrochim. Acta.*, 2005, **51**, 191
- <sup>69</sup> J. K. Zak, J. E. Butler and G. M. Swain, *Anal. Chem.* 2001, **73**, 908
- <sup>70</sup> W. Lu and L. Dai, *Carbon Nanotube Supercapacitors*, INTECH Open Access Publisher, Croatia, 2010, 563

- 
- <sup>71</sup> H. Shiomi, *Jpn. J. Appl. Phys.*, 1997, **36**, 7745
- <sup>72</sup> B. J. M. Hausmann, K. Mughees, Y. Zhang, T. M. Babinec, K. Martinick, M. McCutcheon, P. Hemmer and M. Lončar, *Diamond Relat. Mater.*, 2010, **19**, 621
- <sup>73</sup> S. Yu, N. Yang, H. Zhuang, J. Meyer, S. Mandal, O. A. Williams, I. Lilge, H. Schönherr and X. Jiang, *J. Phys. Chem. C*, 2015, **119**, 18918
- <sup>74</sup> F. Gao and C. E. Nebel, *ACS Appl. Mater. Interfaces.*, 2015, A
- <sup>75</sup> Y. Ando, Y. Nishibayashi and A. Sawabe, *Diamond Relat. Mater.*, 2004, **13**, 633
- <sup>76</sup> E. S. Baik, Y. J. Baik, S. W. Lee and D. Jeon, *Thin Solid Films*, 2000, **377**, 295
- <sup>77</sup> B. I. Kharisov, O. V. Kharissova and U. O. Méndez, *Handbook of Less-Common Nanostructures*, CRC Press, Boca Raton, 2012
- <sup>78</sup> H. Masuda, M. Watanabe, K. Yasui, D. Tryk, T. Rao and A. Fujishima, *Adv. Mater.*, 2000, **12**, 444
- <sup>79</sup> H. Li, S. Cheng, J. Li and J. Song, *J. Nanomater.*, 2015, **2015**, 1
- <sup>80</sup> N. Yang, H. Uetsuka and C. E. Nebel, *Adv. Funct. Mater.*, 2009, **19**, 887
- <sup>81</sup> C. Lu, Y. Li, S. Tian, W. Li, J. Li and C. Gu, *Microelectron. Eng.*, 2011, **88**, 2319
- <sup>82</sup> Y. Yang, M. Yuen, X. Chen, S. Xu, Y. Tang and W. Zhang, *CrystEngComm*, 2015, **17**, 2791
- <sup>83</sup> C. Y. Li and A. Hatta, *Diamond Relat. Mater.*, 2005, **14**, 1780
- <sup>84</sup> C. Y. Li and A. Hatta, *Diamond Relat. Mater.*, 2006, **15**, 357
- <sup>85</sup> C. Y. Li and A. Hatta, *Jpn. J. Appl. Phys.*, 2006, **45**, 8378
- <sup>86</sup> S. W. Lee, Y. J. Baik, C. J. Kang and D. Jeon, *Appl. Surf. Sci.*, 2003, **215**, 265
- <sup>87</sup> D. Luo, L. Wu and J. Zhi, *ACS Nano*, 2009, **3**, 2121
- <sup>88</sup> Q. Yang, W. Chen, C. xiao, A. Hirose and R. Sammynaiken, *Diamond Relat. Mater.*, 2005, **14**, 1683
- <sup>89</sup> H. Zanin, P. W. May, D. J. Fermin, D. Plana, S. M. C. Vieira, W. I. Milne and E. J. Corat, *ACS Appl. Mater. Interfaces*, 2014, **6**, 990
- <sup>90</sup> G. Piret, C. Hébert, J. Mazellier, L. Rousseau, E. Scorsone, M. Cottance, G. Lissorgues, M. O. Heuschkel, S. Picaud, P. Bergonzo and B. Yvert, *Biomaterials*, 2015, **53**, 173
- ABREVIATION?

<sup>91</sup> K. Peng, Y. Yan, S. Gao and J. Zhu, *Adv. Mater.*, 2002, **14**, 1097

<sup>92</sup> N. Yang, *Novel Aspects of Diamond From Growth to Applications*, Springer International Publishing, Switzerland, 2015

<sup>93</sup> S. Furuyama, K. Tahara, T. Iwasaki, M. Shimizu, J. Yaita, M. Kondo, T. Koderu and M. Hatano, *Appl. Phys. Lett.*, 2015, **107**, 163102

<sup>94</sup> E. P. Ivanova, J. Hasan, H. K. Webb, V. K. Truong, G. S. Watson, J. A. Watson, V. A. Baulin, S. Pogodin, J. Y. Wang, M. J. Tobin, C. Löbbe and R. J. Crawford, *Small*, 2012, **8**, 2489

<sup>95</sup> E. P. Ivanova, J. Hasan, H. K. Webb, G. Gervinskas, S. Juodkazis, V. K. Truong, A. H. F. Wu, R. N. Lamb, V. A. Baulin, G. S. Watson, J. A. Watson, D. E. Mainwaring and R. J. Crawford, *Nat. Commun.*, 2013, **4**, 2823

<sup>96</sup> S. Wu, F. Zuber, J. Brugger, K. Maniura-Weber and Q. Ren, *Nanoscale*, 2016, **8**, 2620

<sup>97</sup> S. Praver and R. J. Nemanich, *Philos. Trans. R. Soc. London.*, 2004, **362**, 2537

<sup>98</sup> M. N. Dickson, E. I. Liang, L. A. Rodriguez, N. Vollereaux and A. F. Yee, *Biointerphases*, 2015, **10**, 021010